ARTICLES
https://doi.org/10.1038/s41565-021-00897-1
nature nanotechnology

Check for updates

Therapeutically reprogrammed nutrient signalling enhances nanoparticulate albumin bound drug uptake and efficacy in KRAS-mutant cancer

Ran Li[1,2], Thomas S. C. Ng[1,2], Stephanie J. Wang[1,3], Mark Prytyskach[1], Christopher B. Rodell[1,4], Hannes Mikula[1,5], Rainer H. Kohler[1], Michelle A. Garlin[1], Douglas A. Lauffenburger[3], Sareh Parangi[6], Daniela M. Dinulescu[7], Nabeel Bardeesy[8], Ralph Weissleder[1,2,9] ✉ and Miles A. Miller[1,2] ✉

Nanoparticulate albumin bound paclitaxel (nab-paclitaxel, nab-PTX) is among the most widely prescribed nanomedicines in clinical use, yet it remains unclear how nanoformulation affects nab-PTX behaviour in the tumour microenvironment. Here, we quantified the biodistribution of the albumin carrier and its chemotherapeutic payload in optically cleared tumours of genetically engineered mouse models, and compared the behaviour of nab-PTX with other clinically relevant nanoparticles. We found that nab-PTX uptake is profoundly and distinctly affected by cancer-cell autonomous RAS signalling, and RAS/RAF/MEK/ERK inhibition blocked its selective delivery and efficacy. In contrast, a targeted screen revealed that IGF1R kinase inhibitors enhance uptake and efficacy of nab-PTX by mimicking glucose deprivation and promoting macropinocytosis via AMPK, a nutrient sensor in cells. This study thus shows how nanoparticulate albumin bound drug efficacy can be therapeutically improved by reprogramming nutrient signalling and enhancing macropinocytosis in cancer cells.

Albumin fuels macropinocytosis-driven catabolism in cancer cells[1], and past reports have found that tumour macropinocytosis is regulated by signalling through activated RAS[2], as well as numerous other environmental cues, cell-surface proteins and signalling molecules including RAC/PAK1 (refs. [3,4]). Partly to take advantage of this behaviour, as well as the prevalence of albumin-binding glycoproteins gp60 on endothelial cells and secreted protein acidic and cysteine rich (SPARC) in tumour tissues[5], albumin formulation has been used to improve tumoural drug delivery[6], especially in cancers with constitutively activating RAS mutations. Nab-paclitaxel (nab-PTX, Abraxane) is the first FDA-approved chemotherapy incorporating albumin into its formulation[5], is the highest selling nanomedicine in past 5 years (refs. [7,8]) and is used in treating diseases including metastatic non-small cell lung adenocarcinoma (NSCLC)[9] and metastatic pancreatic ductal adenocarcinoma (PDAC)[10], which are malignancies with high rates of *KRAS* mutation[11]. Nonetheless, the impact of albumin formulation on efficacy has been mixed in clinical trials[12], and there has been little direct, mechanistic evidence of how such albumin-nanoformulation strategies affect the distribution, cellular uptake and activity of drug payloads within the spatially heterogeneous tumour microenvironment (TME) in vivo.

The distribution and uptake of albumin are governed by multiple competing processes throughout the body, and it has been difficult to understand what the true rate-limiting processes are in determining the ultimate fate and action of nab-PTX. For example, SPARC has been proposed as a biomarker[13], but Ph3 trials[14] and genetic experiments proved disappointing[15]. Alternatively, tumour associated macrophages (TAMs) accumulate nab-PTX[16], but their relative importance compared to cancer-cell uptake remains unclear. It therefore is still uncertain what role cancer-cell autonomous macropinocytosis plays in nab-PTX delivery.

Single-cell quantification of nab-PTX biodistribution

To address these issues, here we applied confocal microscopy and tissue clearing techniques to image the delivery and cellular uptake of nab-PTX in mouse models of *KRAS*-mutant NSCLC and PDAC at a single-cell resolution. Nab-PTX is based on the high-pressure homogenization of paclitaxel (PTX) with albumin, forming roughly 130 nm nanoparticles (NPs). We developed a two-colour imaging strategy based on AlexaFluor555-labelled albumin and a fluorescent taxane payload (SiR-taxane; Fig. 1a), yielding a fluorescently labelled laboratory-made nab-PTX formulation with size, charge, characteristics of disaggregation, morphology, in vivo drug target, biodistribution and tumoural accumulation similar to that of commercially available pharmacy-grade nab-PTX (Supplementary Fig. 1). PTX stabilizes microtubules and SiR-taxane fluorescence enhances ten-fold on microtubule binding[17], thus reporting target engagement in vivo. We co-imaged nano-albumin (nab-A555) and its payload (SiR-taxane) in the KP1.9 cell line derived from

[1]Center for Systems Biology, Massachusetts General Hospital Research Institute, Boston, MA, USA. [2]Department of Radiology, Massachusetts General Hospital and Harvard Medical School, Boston, MA, USA. [3]Department of Biological Engineering, Massachusetts Institute of Technology, Cambridge, MA, USA. [4]School of Biomedical Engineering, Science and Health Systems, Drexel University, Philadelphia, PA, USA. [5]Institute of Applied Synthetic Chemistry, Vienna University of Technology (TU Wien), Vienna, Austria. [6]Department of Surgery, Massachusetts General Hospital, Boston, MA, USA. [7]Division of Women's and Perinatal Pathology, Brigham and Women's Hospital, Harvard Medical School, Boston, MA, USA. [8]MGH Cancer Center, Massachusetts General Hospital Research Institute, Boston, MA, USA. [9]Department of Systems Biology, Harvard Medical School, Boston, MA, USA. ✉e-mail: rweissleder@mgh.harvard.edu; miles.miller@mgh.harvard.edu

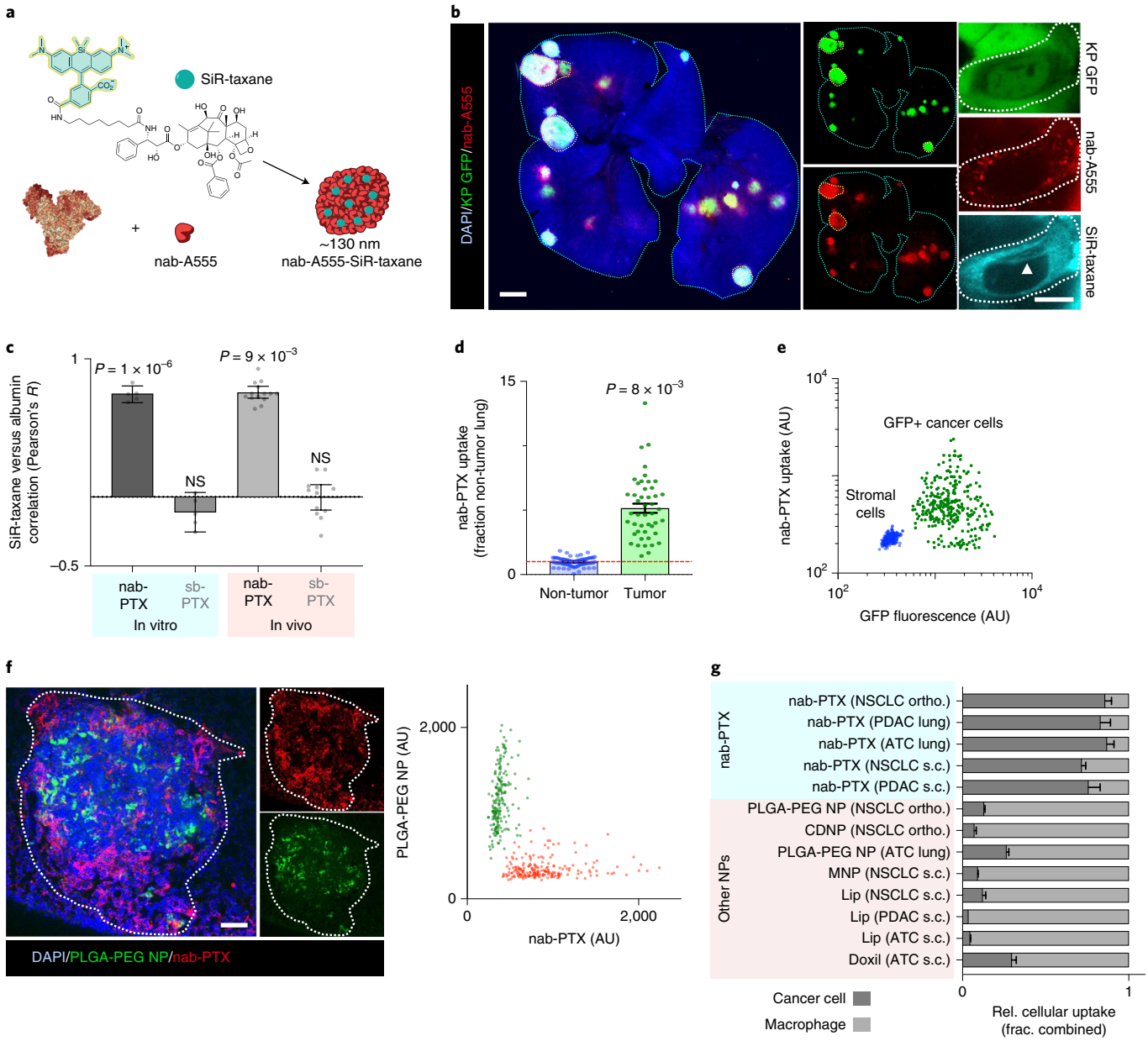

Fig. 1 | Nab-PTX accumulates in cancer cells distinctly from other nanoformulations. a, Schematic for imaging the albumin carrier (nab-A555) and the drug payload (SiR-taxane) of nab-PTX (albumin from Protein Data Bank accession no. 1E7I). **b**, Representative confocal microscopy of nab-PTX in lungs of C57BL/6 mice bearing KP-GFP tumours, 24 h post i.v. administration, at both whole-lung and single-cell levels (left and right scale bars, 2 mm and 10 μm, respectively). Blue, yellow and white lines outline lung, tumour and cancer cells, respectively. Arrow highlights SiR-taxane microtubule binding. **c**, Albumin and PTX uptake were quantified by microscopy and correlated across individual cells either in vitro or from tumour-bearing lungs as in **b** ($n = 413$ cells across four conditions, means ± 95% confidence interval (CI), two-tailed t-test for Pearson's correlation). sb-PTX, solvent-based PTX. **d**,**e**, As in **b**, nab-PTX uptake in tumour tissues (**d**; coefficient of variance, CV = 47%) or GFP-expressing cancer cells (**e**, CV = 74%) was quantified by microscopy (means ± s.e.m. from $n = 6$ lungs). **f**, Confocal images (scale bar, 100 μm) and quantification ($n = 397$ cells from five lungs) of co-dosed nab-PTX and PLGA-PEG NPs in the KP model at 24 h. AU, arbitrary unit. **g**, Confocal microscopy (Supplementary Fig. 3) quantification of nab-PTX and model NPs in cancer cells versus macrophages in orthotopic (ortho.), subcutaneous (s.c.) or lung metastasis (lung) mouse tumour models. In **g**: CDNP, cyclodextrin nanoparticle; MNP, ferumoxytol magnetic nanoparticle; Lip, liposome; Doxil, PEGylated liposomal Dox; ATC, anaplastic thyroid cancer. Data are means ± s.e.m. from $n = 12$–300 cells from $n = 3$ tumours from $n = 3$ mice per condition. Two-tailed t-tests are used for all comparisons. For **b** and **f**, images are representative from four independent experiments with similar results.

the $Kras^{G12D/+}p53^{-/-}$ mouse model of lung adenocarcinoma[18]. In vitro, cellular uptake of nab-A555 correlated with SiR-taxane on a cell-by-cell level, not observed when albumin and SiR-taxane were added separately (Fig. 1c and Supplementary Fig. 2a), therefore suggesting that payload activity depends on nab formulation uptake. We imaged the in vivo distribution of nab-PTX using the orthotopic KP1.9 model in syngeneic C57BL/6 hosts. Optical clearing with CUBIC (clear, unobstructed brain/body imaging cocktails) reagents did not diminish the fluorescent intensity of nab-PTX (Supplementary Fig. 2b), but enabled quantification through

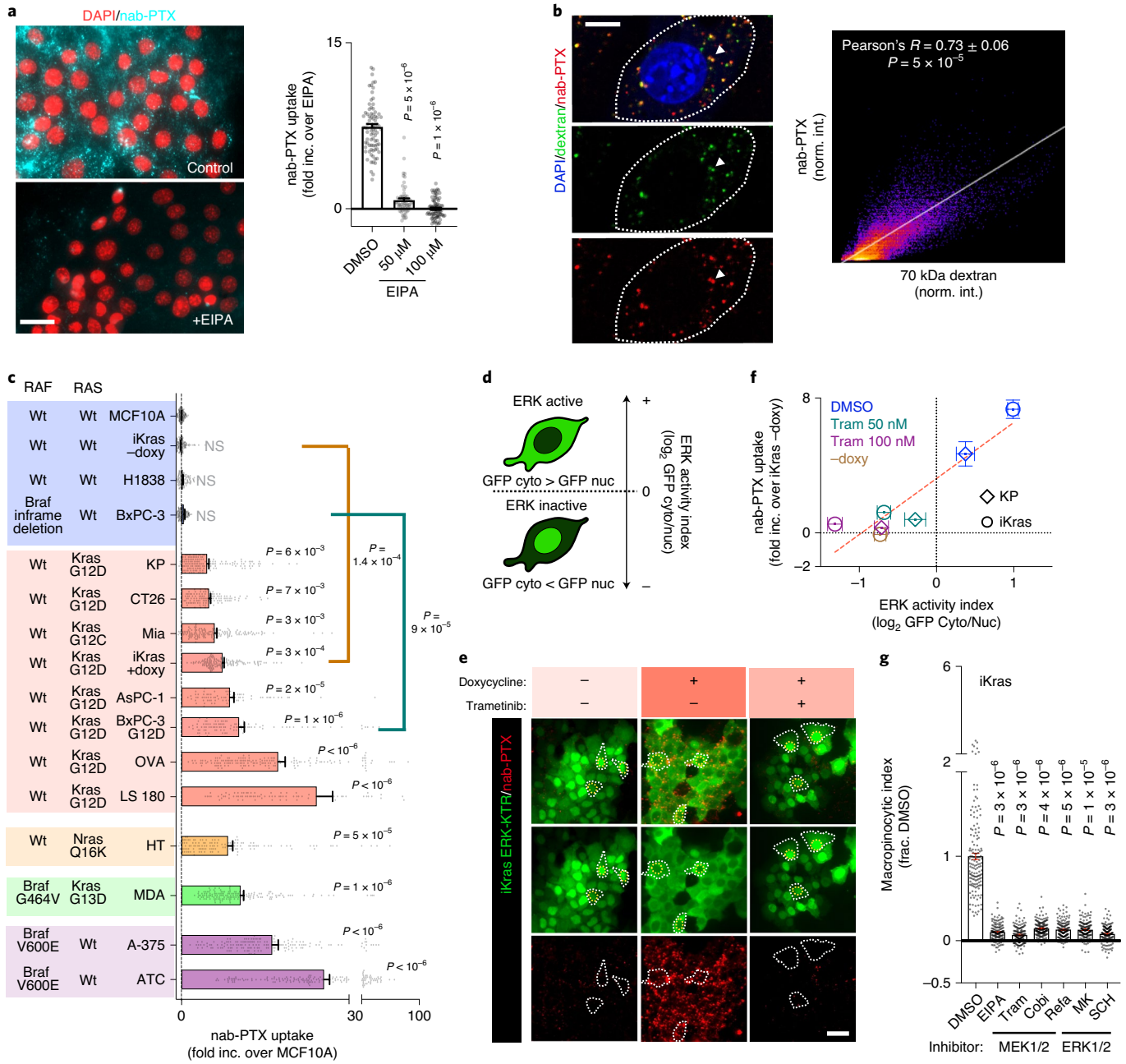

Fig. 2 | RAS signalling drives nab-PTX uptake by cancer cells. a, Representative fluorescence microscopy (scale bar, 10 μm) and quantification (means ± s.e.m., one-way ANOVA/Tukey compared to DMSO) of 4 h nab-PTX uptake by KP cells treated with EIPA for 6 h ($n = 228$ cells across all conditions). **b**, Images (scale bar, 5 μm, white line outlines cancer-cell, white arrow points to colocalization) and pixel-by-pixel quantification ($n = 30$ cells, Pearson's correlation R, means ± 95% CI, two-tailed t-test) of colocalization between 70 kDa dextran signals and nab-PTX in KP cells in vitro. **c**, Quantification of 4 h nab-PTX uptake in cancer or epithelial cell lines ($n = 2{,}305$ cells across all conditions; means ± s.e.m., one-way ANOVA/Holm compared to MCF10A or two-tailed t-test as specified). Wt, wild-type. **d**–**f**, Schematic of ERK-KTR imaging (**d**) and representative images (**e**, iKras; scale bars, 10 μm) and corresponding averaged (**f**, $n = 923$ cells across all conditions, means ± 95% CI) quantification of ERK-KTR and 4 h nab-PTX uptake in cells treated for 24 h with trametinib (tram) and/or doxycycline (doxy). iKras cells were treated with doxy except for '–doxy', denoting 5 day doxy withdrawal. **g**, Quantification of the 70 kDa dextran (Dex) uptake, as a measurement of macropinocytic activity[2], in iKras cells treated with EIPA, MEK inhibitors (tram, trametinib; cobi, cobimetinib; refa, refametinib) and ERK inhibitors (MK, MK-8353; SCH, SCH772984). Data are means ± s.e.m. from $n = 909$ cells across all conditions (one-way ANOVA/Tukey compared to DMSO). norm. int., normalized intensity; frac. ctrl., fraction control; fold inc. over ctrl., fold increase over control.

whole tumour-bearing lungs (Fig. 1b)[19]. Nab-PTX uptake on a cell-by-cell level spatially correlated between nanoparticulate albumin and its taxane payload (Fig. 1b,c and Supplementary Fig. 2c). Nab-PTX accumulated five-fold higher in tumours compared to non-tumour lung, and a large portion of uptake was in cancer cells (Fig. 1d,e). A Cremophor-EL formulation of SiR-taxane (as used with clinical solvent-based sb-PTX formulations) injected separately from A555-labelled albumin (Alb-A555) showed minimal tumour-selective uptake and no correlation between albumin and SiR-taxane (Fig. 1c and Supplementary Fig. 2c,d), probably because

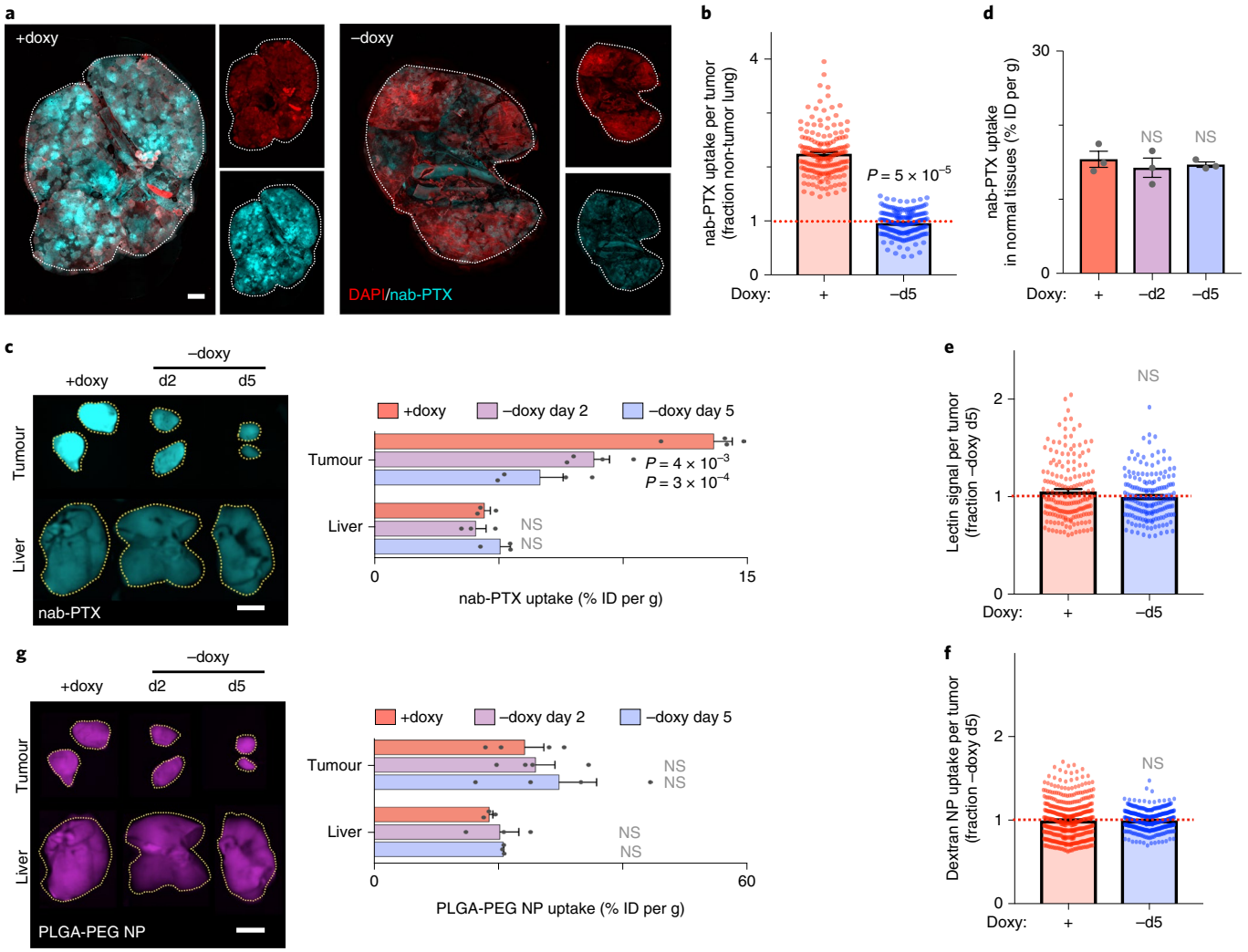

Fig. 3 | Cancer-cell RAS signalling drives in vivo tumour accumulation of nab-PTX. On formation of iKras lung metastases or s.c. tumours, C57BL/6 mice were withdrawn from doxy for either 2 or 5 days, treated with fluorescent nab-PTX, dissected and imaged 24 h posttreatment. **a**,**b**, Representative confocal microscopy (**a**, scale bar, 2 mm) and quantification (**b**) of nab-PTX uptake in the iKras lung tumour. **c**, Representative fluorescent reflectance imaging (left, scale bar, 5 mm) and quantification (right) of tumour and liver uptake of nab-PTX in the iKras s.c. tumour model. **d**, 24 h nab-PTX uptake was combined across all non-tumour organs. **e**,**f**, Lectin (**e**) and dextran-NP uptake (**f**) were quantified in lung tumours. **g**, Co-injected with nab-PTX in **c**, PLGA-PEG NP was i.v. injected into mice bearing iKras s.c. tumours and quantified 24 h later by FRI to measure tumour and liver uptake. For **c**, **d** and **g**, data are means ± s.e.m. from $n = 3$ mice per group (one-way ANOVA/Tukey compared to +doxy). For **b** and **e**, data are means ± s.e.m. from $n = 180$ lung tumours from $n = 3$ animals per condition (two-tailed t-test). For **f**, data are means ± s.e.m. from $n = 804$ tumours from $n = 8$ animals across two conditions (two-tailed t-test). For **b**, **e** and **f**, each data point represents a tumour. For **a**, **c** and **g**, images are representative from three independent experiments with similar results.

Cremophor-EL is known to reduce taxane albumin binding[20]. Thus, accumulation of nab-PTX directs the selective uptake of its taxane payload in orthotopic lung tumours.

We next examined the degree to which nab-PTX delivery merely reflected the general process of passive macromolecular accumulation via factors related to the enhanced permeability and retention (EPR) effect. We compared the distribution of nab-PTX with that of a co-administered model PLGA-PEG polymeric nanoparticle (PLGA-PEG NP) with similarities to clinical PTX formulations such as genexol-PM, and a modest correlation was observed on a tumour-by-tumour basis (Supplementary Fig. 2e). This suggests that nab-PTX tumour uptake is still governed by non-specific effects including EPR and possibly endothelial transcytosis, the latter is known to mediate intratumoural extravasation of albumin[5] and NPs[21]. Yet the overlap between nab-PTX and PLGA-PEG NP uptake on a single-cell level was minimal (Fig. 1f). TAMs play substantial roles in nanomaterial accumulation, and we observed that nab-PTX can indeed accumulate in TAMs, as found previously[16]. Furthermore, cancer cells and macrophages accounted for roughly 92 ± 4% (mean ± 95% CI from $n = 4$ tumours) of nab-PTX uptake in the TME. However, nab-PTX was taken up at highest levels in cancer cells, and in contrast, other model nanoformulations—including polymeric micelles, liposomes and dextran-based NPs including the FDA-approved ferumoxytol—accumulated at highest levels in TAMs (Fig. 1g and Supplementary Fig. 3a–g). This finding was corroborated in vitro with nab-PTX, which disaggregates to particles of roughly 10 nm diameter on dilution (Supplementary Fig. 1a), showing higher uptake in cancer cells compared to macrophages. By contrast, polymeric NPs (roughly 70 nm diameter), as well as nab-PTX that is covalently cross-linked to prevent disaggregation (roughly 160 nm diameter), were taken up at a higher level in macrophages (Supplementary

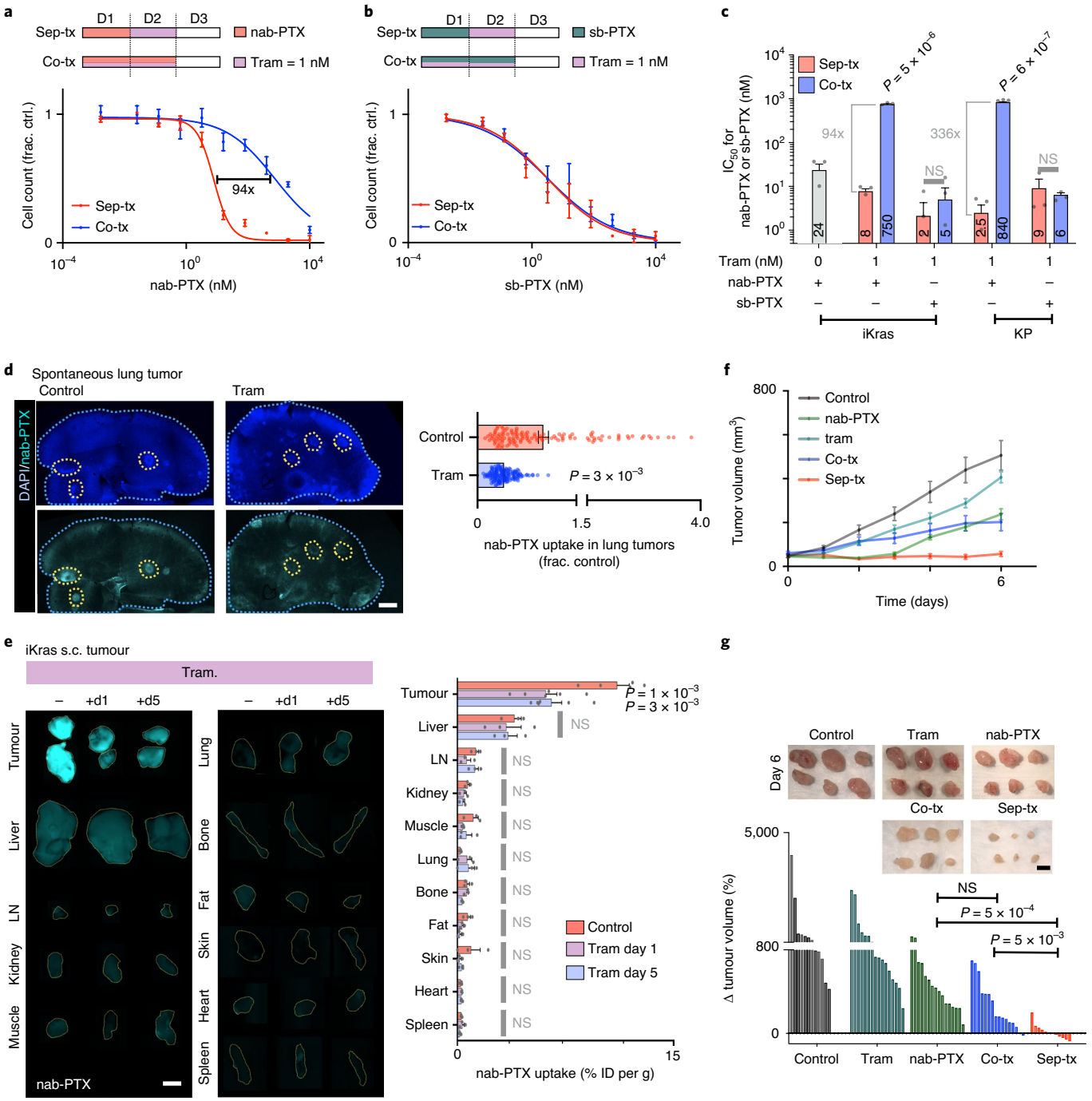

Fig. 4 | MEK1/2 inhibition via trametinib reduces nab-PTX uptake and efficacy. a–c, Treatment schedule and viability of iKras cells receiving either simultaneous (Co-Tx) or sequential (Sep-Tx) treatment of trametinib (tram) and nab-PTX (**a**) or sb-PTX (**b**) in vitro, measured by cell count at 72 h. IC_{50} values are compared across treatments (**c**, IC_{50} value displayed in each bar). **d**, 129S mice bearing $Kras^{G12D/+}p53^{-/-}$ autochthonous lung tumours were pretreated with tram or vehicle control, followed by i.v. nab-PTX injection and 24 h later analysed by CUBIC clearing and confocal imaging for nab-PTX uptake in lung tumours (visualized by DAPI staining). Left, representative images, blue and yellow lines outline the lung and tumours, respectively (scale bar, 2 mm); right, quantification (data are means ± s.e.m. for $n = 265$ tumours from seven mice across two conditions, two-tailed *t*-test). **e**. C57BL/6 mice bearing s.c. iKras tumours were treated with tram, nab-PTX and/or vehicle controls, and 24 h later were analysed by fluorescent reflectance imaging for nab-PTX (**e**; scale bar, 5 mm). **f**, Mice bearing iKras s.c. tumours were treated with vehicle controls, nab-PTX, tram, nab-PTX/tram Co-Tx or Sep-Tx (nab-PTX followed by tram) with equal cumulative doses, and tumour volume was monitored over time by caliper. **g**, Representative images of tumour size (scale bar, 5 mm) and quantification at 6 days posttreatment are shown (bars denote individual tumours). For **a**–**c**, $n = 3$ independent experiments per condition (two-tailed *t*-test); for **e**, $n = 3$ animals per condition (one-way ANOVA/Tukey compared to control). For **f**,**g**, $n = 12$ tumours from $n = 6$ animals per condition (one-way ANOVA/Tukey). Data are means ± s.e.m for all except **g**. For **d**–**g**, the controls are tumour-bearing animals treated via i.v. injection with PBS (vehicle control for nab-PTX) and/or oral gavage with methylcellulose + tween 20 (vehicle control for tram).

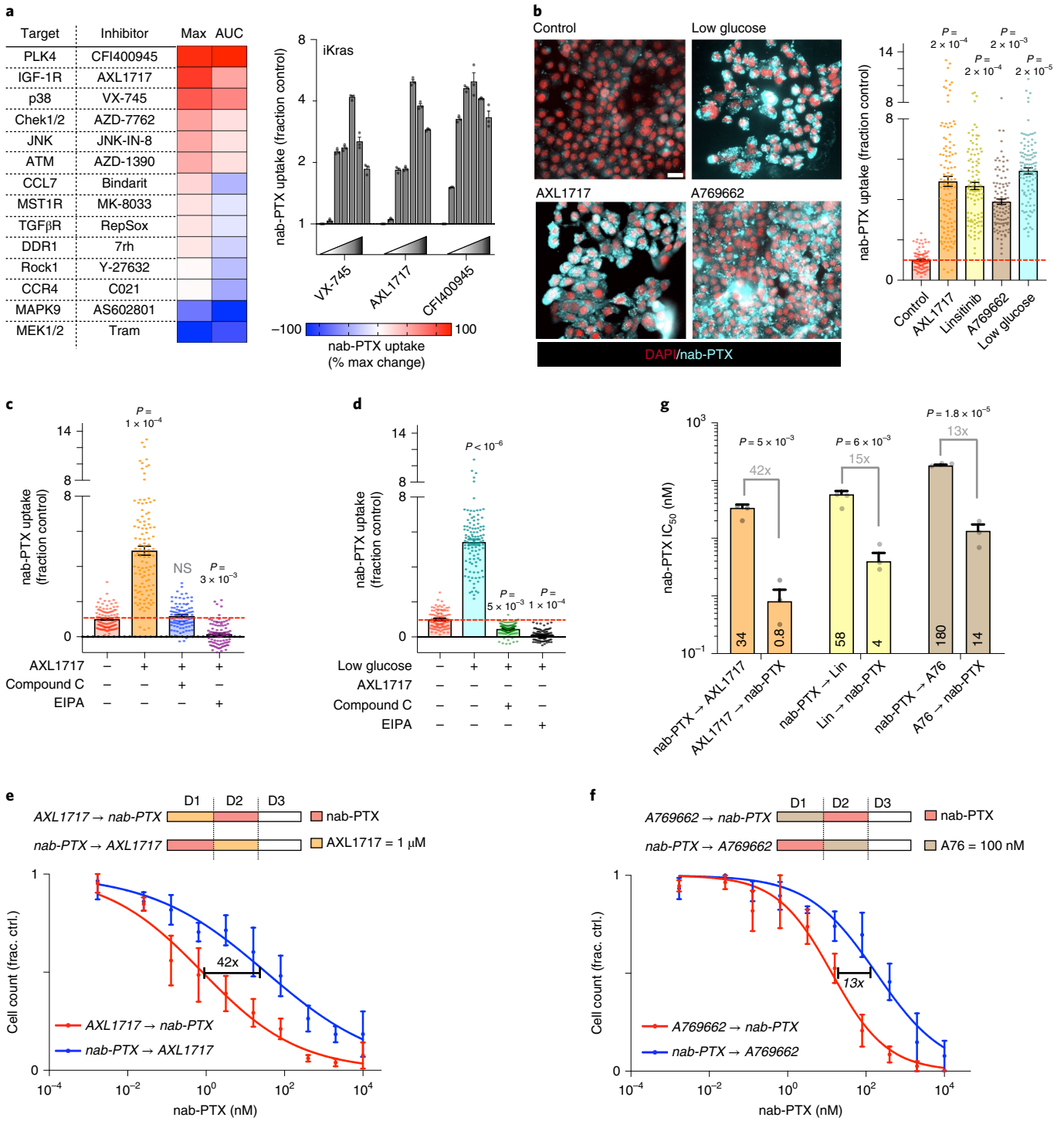

Fig. 5 | IGF1R inhibitor enhances uptake of nab-PTX in an AMPK- and macropinocytosis-dependent manner. a, A targeted screen tested the ability of drugs to enhance nab-PTX uptake in KP and iKras cancer cells across a six-point dose response (means ± s.e.m., $n = 3$), from which maximum change (max) and area under the curve (AUC) were calculated and averaged across both cell types. **b**–**d**, Representative images (**b**, scale bar, 10 μm) and quantification of nab-PTX uptake (**b**, $n = 522$ cells; **c**, $n = 404$ cells, **d**, $n = 417$ cells across all conditions) in treated iKras cells (control, DMSO). Data are means ± s.e.m. (one-way ANOVA/Tukey compared to control). **e**–**g**, nab-PTX cytotoxicity in iKras cells treated either before or after with AXL1717 (**e**), linsitinib (Lin), or A-769662 (A76, **f**), measured at 72 h by resazurin-based assay. Data are means ± s.e.m. for $n = 3$ (two-tailed t-test). Data in **g** (IC_{50} value is displayed in each bar) summarize curves in **e**,**f** and Supplementary Fig. 16.

Fig. 3h,i). These findings indicate that the size of the therapeutics, among other properties, may play a role in determining their relative uptake by cancer cells and macrophages, consistent with previous observations[22].

Mitogen-activated protein kinase (MAPK)/ERK signalling controls nab-PTX uptake by cancer cells

Previous literature has implicated macropinocytosis in the uptake of albumin by *RAS*-mutant cancer cells[2], and we found that the

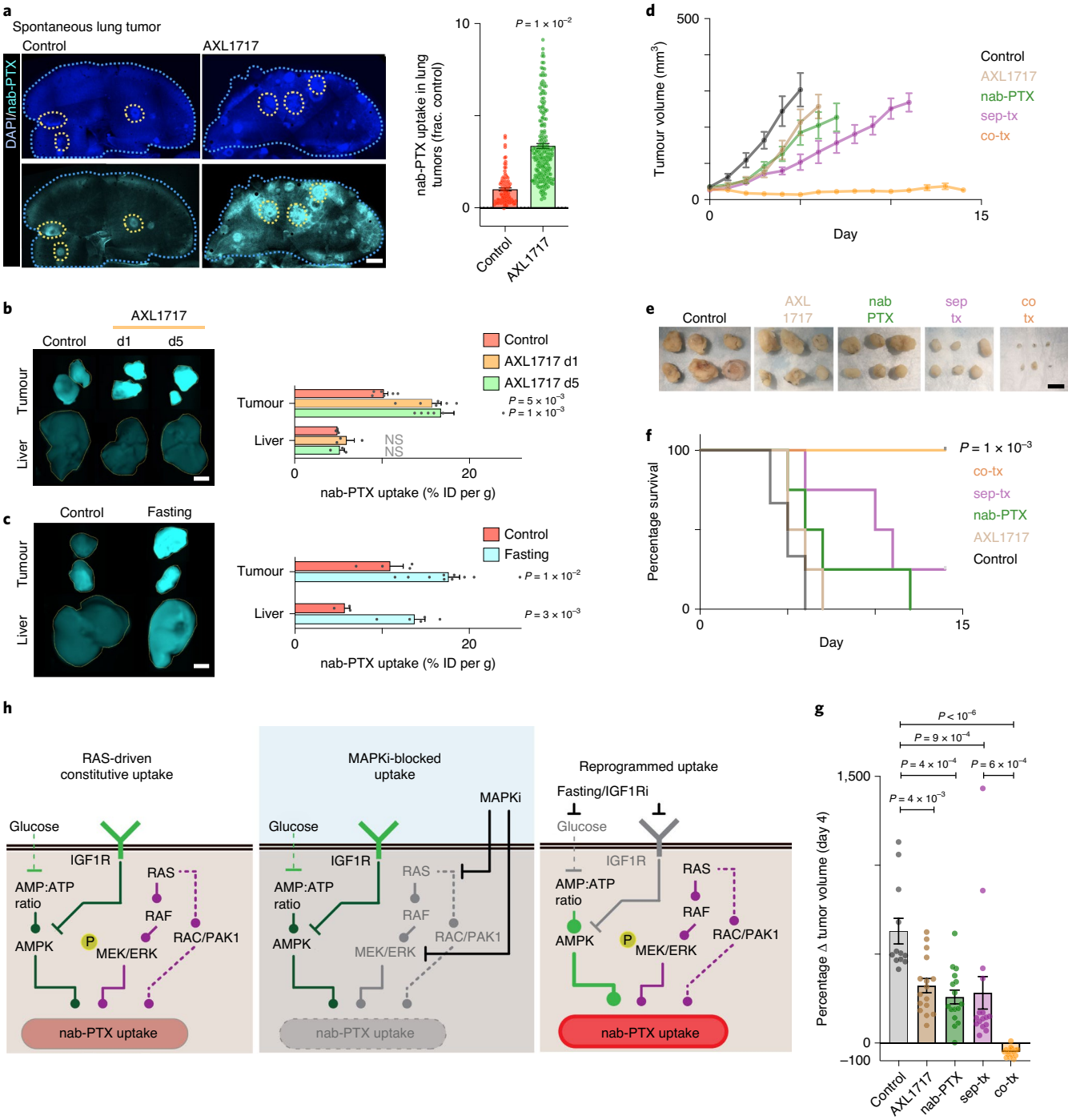

Fig. 6 | IGF1R-targeted kinase inhibitor enhances nab-PTX uptake and efficacy in vivo. a, 129S mice bearing *Kras*$^{G12D/+}$*p53*$^{-/-}$ autochthonous lung tumours were pretreated with AXL1717 or vehicle (reshown control, Fig. 4d), followed by i.v. nab-PTX injection and 24 h later analysed by CUBIC clearing and confocal imaging for nab-PTX uptake in lung tumours (visualized by DAPI staining). Left, representative images, blue and yellow lines outline the lung and tumours, respectively (scale bar, 2 mm); right, quantification (data are means ± s.e.m. for $n = 329$ tumours from eight animals across two conditions; two-tailed *t*-test). **b**,**c**, Animals bearing s.c. iKras tumours were treated with AXL1717 (**b**, control, vehicle control) or fasted (**c**, control, normal diet), nab-PTX was i.v. injected and biodistribution was measured 24 h later by fluorescent reflectance imaging. Representative images (left, scale bar, 5 mm) and quantification (right) show the impact of AXL1717 (**b**) and fasting (**c**) on nab-PTX accumulation. For **b** and **c**, data are means ± s.e.m. for $n = 3$ animals per group (**b**, one-way ANOVA/Tukey compared to control; **c**, two-tailed *t*-test). **d**–**g**, Mice bearing s.c. iKras tumours were treated with vehicle controls, nab-PTX, AXL1717, simultaneous treatment of both (Co-tx) or sequential treatment of both (Sep-tx) with equal cumulative doses. Tumour volume (**d**,**e**) and survival based on humane endpoint (**f**, $n = 4$ per group, log-rank test) were monitored. Representative images of tumour size (**e**, scale bar, 5 mm), as well as percentage change in tumour volume (**g**), are displayed. For **d** and **g**, data are means ± s.e.m from $n = 12$ tumours from six mice per condition (one-way ANOVA/Tukey). For **a**–**g**, the controls are tumour-bearing animals treated i.v. with PBS (vehicle control for nab-PTX) and/or i.p. with olive oil (vehicle control for AXL1717). **h**, Proposed mechanisms for effects of MEK1/2 and IGF1R inhibitors on nab-PTX uptake. MAPKi, such as trametinib or mutant RAS silencing, can reduce nab-PTX uptake by inhibiting the activity of RAS/RAF/MEK/ERK or RAS/RAC/PAK1 pathways[3]. Fasting and IGF1R inhibitor can enhance uptake by promoting AMPK signalling.

macropinocytosis inhibitor 5-(*N*-ethyl-*N*-isopropyl)amiloride (EIPA) eliminated nab-PTX uptake in KP1.9 cells (Fig. 2a). Punctate subcellular colocalization of nab-PTX with fluorescent dextran, dequenched BSA and endolysosomal markers RAB5A, RAB7A and LAMP1 further supported uptake via macropinocytosis and subsequent catabolic degradation in cells (Fig. 2b and Supplementary Fig. 4a–d). Further imaging suggested that taxane from nab-PTX dissociated from albumin vehicle before microtubule target engagement (Supplementary Fig. 4e–f). Nab-PTX uptake was 5–25-fold greater in *RAS*-mutant cancer cells compared to wild-type *RAS* comparators (Fig. 2c and Supplementary Fig. 5a), and uptake correlated between albumin and its drug payload (Supplementary Fig. 5b,c). Transient $KRAS^{G12D}$ over-expression in *KRAS-wt* BxPC-3 PDAC cells, and doxycycline induction of $Kras^{G12D}$ expression in genetically engineered mouse *tetO-*$Kras^{G12D}$ $p53^{-/-}$ PDAC (iKras) cells, both enhanced nab-PTX uptake by ≥8-fold (Fig. 2c and Supplementary Fig. 5d,e). High uptake was also seen in $BRAF^{V600E}$ mutant cells, and both *BRAF* and *KRAS* mutation are known to stimulate downstream extracellular signal-regulated kinase (ERK) phosphorylation. Hence, we used a transgenic kinase translocation reporter (ERK-KTR) to monitor ERK activation (Fig. 2d)[23], which revealed correlation between nab-PTX uptake and ERK activity on a cell-by-cell level (Fig. 2e and Supplementary Fig. 6a–c). Inhibition of ERK signalling using either the clinical MEK1/2 inhibitor trametinib (Mekinist), or doxycycline withdrawal to silence upstream $Kras^{G12D}$, both blocked nab-PTX uptake (Fig. 2e,f). Similarly, inhibiting ERK signalling using MEK1/2 or ERK1/2 inhibitors reduced the cancer-cell uptake of 70 kDa dextran (Fig. 2g and Supplementary Fig. 6d–g). Macropinocytosis inhibition with EIPA, and MEK1/2 inhibition with trametinib, also reduced the uptake of covalently cross-linked nab-PTX (Supplementary Fig. 6h). These data collectively indicate that ERK signalling controls macropinocytic uptake of nab-PTX by cancer cells.

We next examined if inhibiting RAS/RAF/MEK/ERK signalling could impact the accumulation of nab-PTX in vivo. Subcutaneous (s.c.) and intravenous (i.v.) inoculation of iKras cells into doxycycline-fed syngeneic C57BL/6 hosts led to tumour formation in the flank and lungs, respectively, and the latter is a frequent site of PDAC metastasis. Selective tumour accumulation of nab-PTX was eliminated as the result of RAS signalling inhibition via doxycycline withdrawal (Fig. 3a–c and Supplementary Fig. 7a–d; imaged by confocal microscopy and/or fluorescence reflectance imaging, FRI), which correlated with decreased ERK signalling (Supplementary Fig. 7e) and decreased uptake of co-administered albumin (Supplementary Fig. 8a). In contrast, doxycycline withdrawal did not change nab-PTX in non-tumour tissues (Fig. 3d), tumour vascularization (Fig. 3e and Supplementary Fig. 8b,c), tumoural accumulation of a cross-linked dextran-NP (Macrin NP)[24] or PLGA-PEG NP (Fig. 3f,g and Supplementary Fig. 8d,e), suggesting cancer-cell autonomous effects. In vitro doxycycline withdrawal decreased nab-PTX uptake (Fig. 2f) and increased the concentration at which nab-PTX inhibited 50% cell count (IC_{50}) by >30-fold (Supplementary Fig. 9a). Similar effects were seen with trametinib: simultaneous nab-PTX and trametinib treatment (Co-tx) increased IC_{50} by >30-fold (Fig. 4a,c and Supplementary Fig. 9b–f). This increase can largely be attributed to reduced cellular uptake of nab-PTX, rather than impacts on cell proliferation that may affect sustained PTX activity as an anti-mitotic, since trametinib had minimal impact on nab-PTX IC_{50} when it was dosed sequentially after nab-PTX treatment (Sep-tx, Fig. 4a,c and Supplementary Fig. 9b–f). Clinically, nab-PTX is frequently used in combination with gemcitabine, and trametinib increased the IC_{50} of a nab-PTX + gemcitabine combination (Supplementary Fig. 9e). No difference in IC_{50} was observed when solvent-based PTX was used or across single-agent controls using the different dose timings (Fig. 4b,c and Supplementary Fig. 9g–j). In vivo, both spontaneously developed autochthonous lung tumours and s.c. xenografts accumulated less nab-PTX when pretreated with trametinib (Fig. 4d,e and Supplementary Figs. 10a and 11a,b), which translated to reduced efficacy: simultaneous treatment with nab-PTX and trametinib was less effective at blocking tumour growth compared to a regimen in which trametinib was administered after nab-PTX (Supplementary Table 1, Fig. 4f,g and Supplementary Fig. 12), but no difference was found in the same comparison but using sb-PTX (Supplementary Table 2 and Supplementary Fig. 13a–f). Consistent with the selective tumoural uptake of nab-PTX compared to sb-PTX (Fig. 1d and Supplementary Fig. 2d), nab-PTX was more efficacious in blocking tumour growth in vivo compared to sb-PTX (Supplementary Fig. 13h), while this difference was not observed in vitro (Supplementary Fig. 13g). Finally, nab-PTX accumulation in non-tumour organs (Fig. 4e and Supplementary Figs. 10b,c and 11b), as well as perfused tumour vasculature and accumulation of dextran-NP in tumours (Macrin NP, Supplementary Figs. 10d–g and 11c–e), did not decrease with trametinib, suggesting reduced nab-PTX uptake was due to a tumour-cell intrinsic change, rather than changes in the ability of macromolecular materials to reach the tumour. Overall, these results demonstrate that the signalling state of cancer cells can substantially impact nab-PTX delivery, therefore making drug response sensitive to the order in which nab-PTX and trametinib are dosed, which could have implications to clinical trials combining MEK1/2 inhibitors and nab-PTX (trametinib + nab-PTX, NCT01192165).

Reprogramming nutrient signalling enhances nab-PTX efficacy

We next tested whether nab-PTX uptake could be therapeutically enhanced to improve efficacy. Guided by a previous genome-wide shRNA screen[25], we tested how 13 compounds affected nab-PTX uptake (Fig. 5a and Supplementary Figs. 14 and 15), and found six hits: CFI400945 (polo-like kinase 4 inhibitor), AXL1717 (IGF1R inhibitor), VX-745 (p38α inhibitor), AZD-7762 (CHK1/2 inhibitor), JNK-IN-8 (JNK1/2/3 inhibitor) and AZD-1390 (ATM kinase inhibitor). Of these, we focused on AXL1717 and IGF1R as a target, since IGF1R-targeted therapies (IGF1Ri) have entered Ph3 clinical trials in NSCLC[26] and IGF1Ri has been shown to synergize with PD-1 blockade[27]. iKras and KP cells express IGF1R (Supplementary Fig. 16a) and two IGF1R inhibitors (IGF1Ri) enhanced nab-PTX uptake by >4-fold: AXL1717 as above, and the Ph3-tested drug linsitinib (OSI-906) (Fig. 5b). Furthermore, IGF1Ri enhanced the macropinocytic activity of cancer cells as measured by the uptake of 70 kDa dextran (Supplementary Fig. 16b), similar to the results obtained for nab-PTX.

We hypothesized that IGF1Ri enhanced macropinocytic nab-PTX uptake by modulating AMP-activated protein kinase (AMPK), since AMPK is a key regulator of metabolism and nutrient signalling, its activation is linked to catabolism and macropinocytosis[28,29], and IGF1R signalling can downregulate AMPK activity[30,31]. To test this hypothesis, we treated iKras cells with the AMPK activator A769662 (A76), which phenocopied AXL1717 by enhancing nab-PTX uptake (Fig. 5b). We also hypothesized that glucose deprivation could enhance nab-PTX uptake, since it is known to stimulate AMPK[28]. Low glucose culture media also phenocopied AXL1717's effects on nab-PTX uptake (Fig. 5b). Using AMPK inhibitor dorsomorphin (compound C) and the macropinocytosis inhibitor EIPA, we found that AXL1717- and low glucose-mediated enhancements in nab-PTX uptake were both dependent on AMPK activation and macropinocytosis (Fig. 5c,d and Supplementary Fig. 16c). Moreover, both AXL1717 treatment and low glucose culturing condition enhanced the uptake of cross-linked nab-PTX by cancer cells (Supplementary Fig. 17).

Stimulated uptake of nab-PTX enhanced its cytotoxicity. In vitro, pretreatment with AXL1717, A76 or linsitinib improved

(decreased) the IC_{50} of nab-PTX or nab-PTX + gemcitabine, but not sb-PTX, by roughly >5–10-fold (Fig. 5e–g and Supplementary Figs. 16d,e and 18a–d), and controls showed no single-agent dose-timing effects (Supplementary Fig. 18e–i). In vivo, both AXL1717 and animal fasting starting 24 h pre-treatment (Supplementary Figs. 19a and 20a) enhanced the nab-PTX accumulation in autochthonous lung tumours and/or s.c. tumours (Fig. 6a–c). However, fasting also increased nab-PTX in the liver, while AXL1717 did not, suggesting the latter may improve nab-PTX therapeutic index (Fig. 6b,c and Supplementary Figs. 19b,c and 20b,c). Vascular perfusion and accumulation of dextran-NP (Macrin NP) did not change with AXL1717 or fasting (Supplementary Figs. 19d–g and 20d,e), suggesting enhanced nab-PTX delivery was not due to broadly altered EPR effects.

Drug-enhanced nab-PTX uptake translated into improved efficacy in iKras allografts. Alternating treatments with AXL1717 and nab-PTX (Supplementary Table 3), such that the two drugs were separately and sequentially dosed (Sep-tx), only modestly slowed tumour growth compared to monotherapy. However, tumour growth was blocked and survival (time to humane endpoint) was notably extended (despite the limited sample size per group) when simultaneous dosing allowed AXL1717 to enhance nab-PTX uptake (Co-tx, Fig. 6d–g and Supplementary Fig. 21). In contrast, this enhancement in efficacy was not observed using sb-PTX (Supplementary Table 4 and Supplementary Fig. 22). These results show that IGF1R inhibitors can enhance macropinocytosis in an AMPK-dependent manner, similar to glucose deprivation, and improve the accumulation and tumour-killing action of nab-PTX (Fig. 6h).

Conclusion

In summary, we report that the in vivo delivery and action of nab-PTX are affected by RAS signalling state and macropinocytosis in cancer cells. We further demonstrate that therapeutic MAPK inhibition can block the selective delivery and efficacy of nab-PTX, while IGF1Ri enhances its uptake in an AMPK-dependent manner (Fig. 6h). Indeed, a signature of gene expression controlled by MAPK and AMPK signalling output[32,33] correlates with nab-PTX uptake across multiple cancer-cell lines, further suggesting that nab-PTX uptake is controlled by MAPK and AMPK activities (Supplementary Table 5 and Supplementary Fig. 23). Moreover, since both IGF1R and AMPK are key regulators of cell metabolism[28], our results thus indicate that nab-PTX uptake and efficacy can be enhanced by reprogramming nutrient signalling. We also note that while these macropinocytosis- and nutrient signalling-dependent effects apply to cross-linked nab-PTX, they do not extend to sb-PTX (formulated with Cremophor-EL as used clinically), possibly because Cremophor-EL can reduce taxane binding to albumin[20]. Hence, we anticipate generalizability of our findings to other albumin bound drugs including nanotherapies with albumin components[34], albumin-binding prodrugs[35], albumin-fusion biologics[36] and potentially numerous drugs that have high intrinsic affinity for albumin and plasma protein binding, such as the BRAF inhibitors dabrafenib or vemurafenib[37].

Our results have implications to clinical trials using MAPK inhibitors + nab-PTX therapy, and provide rationale for IGF1R inhibitor + nab-PTX combination therapy. We have also demonstrated, through in vitro experiments, that MEK1/2 and IGF1R inhibitors affect the efficacy of nab-PTX + gemcitabine treatment. Future in vivo experiments should test these results in animal models, and provide further evidence on how MAPK/AMPK activities affect nab-PTX + gemcitabine or nab-PTX + oxaliplatin combination therapies. Although here we focus solely on downstream RAS/RAF/MEK/ERK signalling, it is known that nutrient uptake can be stimulated by upstream receptor tyrosine kinases including EGFR and HER2 (ref. [38]). Hence, it is possible that EGFR- and HER2-targeted kinase inhibitors such as erlotinib and lapatinib may similarly impact nab-PTX, pertinent to clinical trials testing their combination (T-DM1 + lapatinib + nab-PTX, NCT02073916; erlotinib + nab-PTX + gemcitabine, NCT01010945). Overall, our results demonstrate the potential impacts of MAPK and nutrient signalling state on nab-PTX action, and we anticipate that the image-based experimental approach used here will be useful in understanding the extent to which this mechanism applies in other cancer types and drug combinations.

Online content

Any methods, additional references, Nature Research reporting summaries, source data, extended data, supplementary information, acknowledgements, peer review information; details of author contributions and competing interests; and statements of data and code availability are available at https://doi.org/10.1038/s41565-021-00897-1.

Received: 18 December 2019; Accepted: 11 March 2021;
Published online: 6 May 2021

References

1. Davidson, S. M. et al. Direct evidence for cancer-cell-autonomous extracellular protein catabolism in pancreatic tumors. *Nat. Med.* **23**, 235–241 (2017).
2. Commisso, C. et al. Macropinocytosis of protein is an amino acid supply route in Ras-transformed cells. *Nature* **497**, 633–637 (2013).
3. Lee, S. W. et al. EGFR-Pak signaling selectively regulates glutamine deprivation-induced macropinocytosis. *Dev. Cell* **50**, 381–392.e5 (2019).
4. Yao, W. et al. Syndecan 1 is a critical mediator of macropinocytosis in pancreatic cancer. *Nature* **568**, 410–414 (2019).
5. Yardley, D. A. nab-Paclitaxel mechanisms of action and delivery. *J. Control. Release* **170**, 365–372 (2013).
6. Hoogenboezem, E. N. & Duvall, C. L. Harnessing albumin as a carrier for cancer therapies. *Adv. Drug Deliv. Rev.* **130**, 73–89 (2018).
7. Barkat, M. A., Beg, S., Pottoo, F. H. & Ahmad, F. J. Nanopaclitaxel therapy: an evidence based review on the battle for next-generation formulation challenges. *Nanomed.* **14**, 1323–1341 (2019).
8. Havel, H. A. Where are the nanodrugs? An industry perspective on development of drug products containing nanomaterials. *AAPS J.* **18**, 1351–1353 (2016).
9. Socinski, M. A. et al. Weekly nab-paclitaxel in combination with carboplatin versus solvent-based paclitaxel plus carboplatin as first-line therapy in patients with advanced non-small-cell lung cancer: final results of a phase III trial. *J. Clin. Oncol.* **30**, 2055–2062 (2012).
10. Von Hoff, D. D. et al. Gemcitabine plus nab-paclitaxel is an active regimen in patients with advanced pancreatic cancer: a phase I/II trial. *J. Clin. Oncol.* **29**, 4548–4554 (2011).
11. Waters, A. M. & Der, C. J. KRAS: the critical driver and therapeutic target for pancreatic cancer. *Cold Spring Harb Perspect. Med.* **8**, a031435 (2018).
12. Tempero, M. A. et al. APACT: phase III, multicenter, international, open-label, randomized trial of adjuvant nab-paclitaxel plus gemcitabine (nab-P/G) vs gemcitabine (G) for surgically resected pancreatic adenocarcinoma. *J. Clin. Oncol.* **37:15**, 4000 (2019).
13. Desai, N., Trieu, V., Damascelli, B. & Soon-Shiong, P. SPARC expression correlates with tumor response to albumin-bound paclitaxel in head and neck cancer patients. *Transl. Oncol.* **2**, 59–64 (2009).
14. Hidalgo, M. et al. SPARC expression did not predict efficacy of nab-paclitaxel plus gemcitabine or gemcitabine alone for metastatic pancreatic cancer in an exploratory analysis of the phase III MPACT trial. *Clin. Cancer Res.* **21**, 4811–4818 (2015).
15. Neesse, A. et al. SPARC independent drug delivery and antitumour effects of nab-paclitaxel in genetically engineered mice. *Gut* **63**, 974–983 (2014).
16. Cullis, J. et al. Macropinocytosis of nab-paclitaxel drives macrophage activation in pancreatic cancer. *Cancer Immunol. Res.* **5**, 182–190 (2017).
17. Lukinavičius, G. et al. Fluorogenic probes for live-cell imaging of the cytoskeleton. *Nat. Methods* **11**, 731–733 (2014).
18. DuPage, M., Dooley, A. L. & Jacks, T. Conditional mouse lung cancer models using adenoviral or lentiviral delivery of Cre recombinase. *Nat. Protoc.* **4**, 1064–1072 (2009).
19. Cuccarese, M. F. et al. Heterogeneity of macrophage infiltration and therapeutic response in lung carcinoma revealed by 3D organ imaging. *Nat. Commun.* **8**, 14293 (2017).
20. Sparreboom, A. et al. Cremophor EL-mediated alteration of paclitaxel distribution in human blood. *Cancer Res.* **59**, 1454–1457 (1999).

21. Sindhwani, S. et al. The entry of nanoparticles into solid tumours. *Nat. Mater.* **19**, 566–575 (2020).
22. Walkey, C. D., Olsen, J. B., Guo, H., Emili, A. & Chan, W. C. Nanoparticle size and surface chemistry determine serum protein adsorption and macrophage uptake. *J. Am. Chem. Soc.* **134**, 2139–2147 (2012).
23. Regot, S., Hughey, J. J., Bajar, B. T., Carrasco, S. & Covert, M. W. High-sensitivity measurements of multiple kinase activities in live single cells. *Cell* **157**, 1724–1734 (2014).
24. Kim, H. Y. et al. Quantitative imaging of tumor-associated macrophages and their response to therapy using ^{64}Cu-labeled macrin. *ACS Nano* **12**, 12015–12029 (2018).
25. Redelman-Sidi, G. et al. The canonical Wnt pathway drives macropinocytosis in cancer. *Cancer Res.* **78**, 4658–4670 (2018).
26. Langer, C. J. et al. Randomized, phase III trial of first-line figitumumab in combination with paclitaxel and carboplatin versus paclitaxel and carboplatin alone in patients with advanced non-small-cell lung cancer. *J. Clin. Oncol.* **32**, 2059–2066 (2014).
27. Ajona, D. et al. Short-term starvation reduces IGF-1 levels to sensitize lung tumors to PD-1 immune checkpoint blockade. *Nat. Cancer* **1**, 75–85 (2020).
28. Hardie, D. G., Ross, F. A. & Hawley, S. A. AMPK: a nutrient and energy sensor that maintains energy homeostasis. *Nat. Rev. Mol. Cell Biol.* **13**, 251–262 (2012).
29. Kim, S. M. et al. PTEN deficiency and AMPK activation promote nutrient scavenging and anabolism in prostate cancer cells. *Cancer Disco.* **8**, 866–883 (2018).
30. Ning, J., Xi, G. & Clemmons, D. R. Suppression of AMPK activation via S485 phosphorylation by IGF-I during hyperglycemia is mediated by AKT activation in vascular smooth muscle cells. *Endocrinology* **152**, 3143–3154 (2011).
31. Tosca, L., Chabrolle, C., Crochet, S., Tesseraud, S. & Dupont, J. IGF-1 receptor signaling pathways and effects of AMPK activation on IGF-1-induced progesterone secretion in hen granulosa cells. *Domest. Anim. Endocrinol.* **34**, 204–216 (2008).
32. Wagle, M. C. et al. A transcriptional MAPK Pathway Activity Score (MPAS) is a clinically relevant biomarker in multiple cancer types. *NPJ Precis Oncol.* **2**, 7 (2018).
33. Wan, L. et al. Phosphorylation of EZH2 by AMPK suppresses PRC2 methyltransferase activity and oncogenic function. *Mol. Cell* **69**, 279–291.e5 (2018).
34. Cui, M. et al. Multifunctional albumin nanoparticles as combination drug carriers for intra-tumoral chemotherapy. *Adv. Health. Mater.* **2**, 1236–1245 (2013).
35. Zaro, J. L. Lipid-based drug carriers for prodrugs to enhance drug delivery. *AAPS J.* **17**, 83–92 (2015).
36. Bush, M. A. et al. Safety, tolerability, pharmacodynamics and pharmacokinetics of albiglutide, a long-acting glucagon-like peptide-1 mimetic, in healthy subjects. *Diabetes Obes. Metab.* **11**, 498–505 (2009).
37. Suo, Z. et al. Investigation on the interaction of dabrafenib with human serum albumin using combined experiment and molecular dynamics simulation: exploring the binding mechanism, esterase-like activity, and antioxidant activity. *Mol. Pharm.* **15**, 5637–5645 (2018).
38. Scaltriti, M. & Baselga, J. The epidermal growth factor receptor pathway: a model for targeted therapy. *Clin. Cancer Res.* **12**, 5268–5272 (2006).

Methods

Cell culture and animal models. *Cell lines and cell culture.* KP1.9 mouse cancer cells (KP, a gift from A. Zippelius, University Hospital Basel), derived from Cre-activated *Kras*$^{LSL-G12D/+}$*Trp53*$^{flox/flox}$ genetically engineered mouse model of lung adenocarcinoma[18], were cultured in Iscove's modified Dulbecco's medium (Invitrogen). AC37 mouse cancer cells with doxycycline-inducible *Kras*^{G12D} expression (iKras, a gift from H. Ying, MD Anderson Cancer Center, by way of N. Bardeesy, Massachusetts General Hospital (MGH)), derived from triple transgenic *p48-Cre;ROSA26-LSL-rtTa-IRES-GFP;TetO-LSL-Kras*^{G12D} genetically engineered mouse model of pancreatic ductal carcinoma[39], were maintained in Dulbecco's Modified Eagle Medium/Nutrient Mixture F-12 media (DMEM/F12, Invitrogen) supplemented with 2 μg ml^{-1} doxycycline (doxy, Sigma). NCI-H1838 human lung adenocarcinoma cells, BxPC-3 human pancreatic adenocarcinoma cells, CT26 mouse colon carcinoma cells and AsPC-1 human pancreatic adenocarcinoma cells were cultured in RPMI1640 media (Corning). Mia PaCa-2 human pancreatic carcinoma cells (Mia), LS 180 human colon adenocarcinoma cells, HT-1080 human fibrosarcoma cells (HT-1080), Raw 264.7 macrophages (Raw), MDA-MB-231 human breast adenocarcinoma cells (MDA) and A-375 human melanoma cells were all cultured in DMEM (Corning). The murine 4306 cancer-cell line (*Kras*^{G12D};*Pten*$^{-/-}$ endometrioid ovarian adenocarcinoma, OVA, from D. Dinulescu, Harvard Medical School), isolated from the Cre-activated *LSL-Kras*$^{G12D/+}$*Pten*$^{loxP/loxP}$ ovarian cancer genetically engineered mouse model[40,41] and 3743 mouse thyroid cancer cells (anaplastic thyroid cancer (ATC), from S. Parangi, MGH), isolated from *Braf*$^{V600E/WT}$*p53*$^{-/-}$ genetically engineered mouse model of anaplastic thyroid tumours[42,43], were also cultured in DMEM. MCF10A human breast epithelial cells were cultured in DMEM/F12 media supplemented with 20 ng ml^{-1} EGF (Peprotech), 0.5 μg ml^{-1} hydrocortisone (Sigma), 100 ng ml^{-1} cholera toxin (Sigma) and 10 μg ml^{-1} insulin (Sigma). Bone marrow-derived macrophages (BMDMs) were isolated from the femurs of 10 weeks old C57BL/6 mice, and maintained in Iscove's modified Dulbecco's medium supplemented with 10 ng ml^{-1} M-CSF (PeproTech). After 6 d of culturing, the BMDMs were subsequently treated with 100 ng ml^{-1} LPS (Sigma) + 50 ng ml^{-1} IFNγ (PeproTech) or 10 ng ml^{-1} IL4 (PeproTech) for polarization toward a proinflammatory M1-like or anti-inflammatory M2-like phenotype, respectively[44]. All growth media were supplemented with 10% foetal bovine serum (Invitrogen) or 5% horse serum (for MCF10A growth media, Invitrogen), 100 IU penicillin, and 100 μg ml^{-1} streptomycin (Invitrogen). All cell lines, except for KP, iKras, OVA and ATC, were obtained from American Type Culture Collection. In some experiments, enhanced green fluorescent protein (eGFP)-expressing versions of KP[19] and ATC[45] cells were used. All cells were cultured at 5% CO_2 and 37 °C in a humidified incubator, and were routinely tested for mycoplasma contamination (PlasmoTest Mycoplasma Detection Kit, InvivoGen).

Animal models. Animal research was performed in compliance with guidelines from the Institutional Animal Care and Use Committee (IACUC) at MGH. Unless otherwise noted, experiments were performed using female mice that were 6–12 weeks old. The 129S1 mice harbouring Cre-activated conditional *Kras*$^{LSL-G12D/+}$*Trp53*$^{flox/flox}$ (129KP mice, a generous gift from M. J. Pittet, MGH) were used as an autochthonous mouse model of non-small cell lung cancer[18]. C57BL/6J (JAX), B6129SF1/J (JAX) and 129KP mice were fed with autoclaved food and water and maintained in ventilated cages in a light–dark cycle, temperature (18–23 °C) and humidity (40–60%) controlled pathogen-free vivarium at MGH. Litter-mates were randomly assigned to experimental groups and the mice underwent procedure and monitoring on the same day in a randomized order.

Method details. *Materials and pharmaceutical agents.* Reagents and solvents were purchased from Sigma-Aldrich and used without further purification, unless otherwise indicated. Water was purified by MilliQ filtration systems (Millipore) before experimental use. Trametinib, gemcitabine and PTX were purchased from LC Laboratories. STEALTH liposomal doxorubicin HCl (Doxil) and DiI-labelled PEGylated DOPC/CHOL liposomes (Lip) were purchased from FormuMax. Pharmacy-grade nanoparticulate albumin bound PTX (nab-PTX, trade name Abraxane; Celgene) was purchased form McKesson (Irving, Taxes). CFI400945 fumarate (CFI400945), AXL1717 (ref. [46]), VX-745, AZD-7762, JNK-IN-8, AZD-1390, Bindarit, MK-8033, AS602801, cobimetinib, refametinib, MK-8353, SCH772984, A-769662, Compound C dihydrochloride (Compound C) and Linsitinib (Lin)[47] were all purchased from MedChemExpress. RepSox, 7rh, Y-27632 dihydrochloride (Y-27632) and C021 dihydrochloride (C021) were purchased from Tocris, Sigma, Abcam and R&D Systems, respectively. EIPA was purchased from Sigma-Aldrich.

Fluorescent dye conjugation. Pharmacy-grade nab-PTX (Abraxane, Celgene) and human serum albumin (Alb, Sigma) were conjugated to AlexaFluor 488 (A488, excitation wavelength (λ_{ex})/emission wavelength (λ_{em}) = 490/525 nm), 555 (A555, $\lambda_{ex}/\lambda_{em}$ = 555/580 nm) or 647 (A647, $\lambda_{ex}/\lambda_{em}$ = 650/665 nm) via *N*-hydroxysuccinimide (NHS) ester chemistry. Briefly, 6 mg of nab-PTX or 5.4 mg of albumin was dissolved in 100 μl sodium bicarbonate buffer (0.1 M, pH 8.2) and mixed with 1 mg of AlexaFluor NHS ester dyes (Invitrogen). The mixture was continuously stirred for 5 h at room temperature at 300 r.p.m. Unreacted AlexaFluor dye was separated from the reaction mixture via centrifugation using 50 kDa (for nab-PTX) or 30 kDa (for Alb) molecular-weight cut-off (MWCO) Amicon centrifugal filter units (Millipore).

BODIPY-TMR-NH_2 (Lumiprobe, $\lambda_{ex}/\lambda_{em}$ = 545/570 nm) was conjugated to poly(D,L-lactide-coglycolide) (PLGA, 50:50 lactide:glycolide, molecular weight 30–60 kDa, Sigma) as described previously[48]. Briefly, 200 mg (0.004 mmol) of PLGA, 16 mg (0.08 mmol) of 1-ethyl-3-(3-dimethylaminopropyl)carbodiimide (EDCI) (Sigma) and 4 mg (0.04 mmol) of NHS (Sigma) dissolved in dimethylformamide (DMF) (Sigma) were mixed with 4 mg (0.009 mmol) of BODIPY-TMR-NH_2 dissolved in *N*,*N*-diisopropylethylamine (DIPEA, 0.04 mmol, Sigma). The mixture was continuously stirred at room temperature in the dark for 24 h. Polymers conjugated to the fluorescent dye (PLGA-BODIPY-TMR) were then purified from unreacted dyes with repeated cycle of precipitation with diethyl ether, followed by centrifugation (2,000*g*, 10 min) and washing in minimal amount of dichloromethane. The red precipitate resulting from the purification step was vacuum dried overnight before dissolving in DMF.

Taxane was conjugated to silicon rhodamine carboxylate (SiR-COOH, $\lambda_{ex}/\lambda_{em}$ = 650/670 nm) as we previously synthesized and characterized[49]. Cross-linked iron oxide NPs (CLIO) and polyglucose (dextran) NPs (Macrin NP) were previously validated and used as in vivo imaging probes for macrophages, as they preferentially accumulate in these cells[24,50]. CLIO and Macrin NP were conjugated to VivoTag 680-NHS (VT680-NHS, Perkin Elmer, $\lambda_{ex}/\lambda_{em}$ = 665/688 nm) according to previously published protocols[24,50]. Cyclodextrin NP (CDNP), a newly designed NP targeting macrophages, was conjugated to A555-NHS ester using NHS ester chemistry following published protocols[44].

NP synthesis and characterization. CLIO was synthesized as described previously[50,51]. Briefly, monodispersed superparamagnetic iron oxide colloid (synthesized in MGH-CSB, US Patent 5,262,176) was reacted with epichlorohydrin (Sigma) to crosslink the dextran coating of the monodispersed superparamagnetic iron oxide colloid. The resulting product was then aminated to produce CLIO.

Macrin NP was synthesized according to previously published protocols[24]. Carboxymethylated polyglucose (TdB Consultancy) activated with EDCI and NHS were mixed with L-lysine (Sigma) dissolved in 2-(*N*-morpholino)ethanesulfonic acid (MES) (Sigma) buffer. The resulting mixture was stirred at room temperature for at least 5 h. Macrin NP was recovered from the reactants by precipitation with ethanol and centrifugation (2,500*g*, 3 min) to produce a white paste. This white paste was dissolved in water and filtered with a 0.22 μm nylon syringe filter, followed by 3-d of dialysis against water with 8–10 kDa MWCO dialysis cassette at room temperature. The resulting product was again filtered with a 0.22 μm syringe filter and lyophilized.

β-CDNP was produced following a previously published protocol[44]. Briefly, succinyl-β-cyclodextrin (CD, Sigma) was mixed with EDCI and NHS in MES buffer and stirred for 30 min. L-lysine was then added and the mixture was stirred overnight at room temperature to crosslink cyclodextrin. The resulting product was recovered by precipitation from ice-cold ethanol and centrifugation at 2,500*g* for 3 min. The precipitant was redissolved in water, filtered with 0.22 μm nylon syringe filter and concentrated with centrifugal filtration using a 10 kDa MWCO Amicon centrifugal filter unit. The final product was lyophilized before future use.

Poly(D,L-lactic-coglycolic acid)-β-polyethylene glycol (PLGA-PEG) NPs were synthesized via nano-precipitation and fluorescently labelled with co-encapsulation of PLGA-BODIPY-TMR[48]. Briefly, 5 mg of PLGA(75:25 lactide:glycolide)$_{8.3kDa}$-PE G$_{5.5kDa}$ (Advanced Polymer Materials, Inc., lot no. 01-13-146-1) and 1 mg of PLGA-BODIPY-TMR was dissolved in 400 μl of DMF:acetonitrile mixture (1:1). The resulting mixture was added drop-wise into 10 ml of water and stirred at room temperature overnight, followed by syringe filtration through a 0.45-μm cellulose acetate filter (Whatman, GE Healthcare). The filtrate was concentrated with a 100 kDa MWCO Amicon centrifugal filter unit (Millipore) operating at 3,000*g* for 30 min to obtain PLGA-PEG NP mixture.

Laboratory-made AlexaFluor555-labelled nanoparticulate albumin bound SiR-labelled PTX (nab-A555-SiR-taxane) was prepared by coupling SiR-taxane to A555-labelled albumin (Alb-A555) via ultrasonic homogenization. Briefly, 1 mg SiR-taxane was dissolved in 64.8 μl of chloroform (Sigma) and 7.2 μl of ethanol. This mixture was combined with 18 mg Alb-A555 dissolved in 3.6 ml of water, and stirred vigorously for 5 min. The resulting mixture was sonicated at 40% amplitude for four cycles (1 min sonication followed by 30 s of pause) using a probe-tip sonicator (QSonica) to produce albumin NPs. Chloroform and ethanol were extracted from the mixture using a Rotavapor (Buchi) operating at 40 °C (ref. [16]). The aqueous mixture was lyophilized to obtain nab-A555-SiR-taxane. In certain experiments, synthesized fluorescent conjugates of nab-PTX were covalently cross-linked by 8% glutaraldehyde and purified via 100 kDa MWCO Amicon centrifugal filter unit following previous protocols[52,53].

The sizes of NPs were characterized by dynamic light scattering using a Zetasizer APS (Malvern): Macrin NP, 17 nm (polydispersity index (PDI), 0.22)[24]; PLGA-PEG NP, 70 nm (PDI, 0.14); CDNP, 25 nm (PDI, 0.24)[44]; magnetic NP (MNP), 34 nm (PDI, 0.13); liposome, 107 nm (PDI, 0.10), Doxil, 84 nm (PDI, 0.02); nab-A555-SiR-taxane, 140 nm (PDI, 0.09); pharmacy-grade nab-PTX, 132 nm (PDI, 0.11); cross-linked nab-A555-SiR-taxane, 167 nm (PDI, 0.34). The zeta-potentials of the particles were determined in PBS using a Zetasizer ZS

(Malvern): Macrin NP, −4 mV (ref. [24]); PLGA-PEG NP, −17.2 mV; CDNP, −10 mV (ref. [44]); MNP, −15.6 mV; liposome = −1 mV; Doxil, −2 mV; nab-A555-SiR-taxane, −13.2 mV; pharmacy-grade nab-PTX, −11.4 mV and cross-linked nab-A555-SiR-taxane, −9.8 mV. When appropriate, pharmacy-grade nab-PTX, nab-A555-SiR-taxane or cross-linked nab-A555-SiR-taxane was diluted to 0.75 mg ml^{-1} nab-PTX (0.075 mg PTX payload per ml) to simulate the dissociation of the NPs in blood[5].

Transmission electron microscope (JEOL 1011) was used to assess NP morphology. Before imaging, NPs were prepared as previously described[48]. Briefly, 10 µl of 15 mg ml^{-1} pharmacy-grade nab-PTX (Abraxane, McKesson) or laboratory-made nab-PTX was deposited on a carbon-coated copper grid. The sample was then stained with a solution of uranyl acetate to provide contrast, and imaged immediately. Finally, encapsulation efficiency and loading capacity of laboratory-made nab-PTX were calculated by measuring the amount of PTX in the NPs with high-pressure liquid chromatography–mass spectrometry, and using the following formula:

- Encapsulation efficiency = (weight of drug in the NP/weight of drug added when making NP) × 100%.
- Loading capacity = (weight of drug in the NP/total weight of NP) × 100%.

On the basis of these formulas, we calculated the encapsulation efficiency and loading capacity of laboratory-made nab-PTX to be 88.5 ± 2.6% and 5.11 ± 0.15% (means ± s.e.m., $n = 3$), respectively.

Cell transfection and transduction. KP and iKras cells expressing Erk kinase translocation mClover (related to GFP) reporter (ERK-KTR) were generated by lentiviral transduction using pLentiCMV Puro DEST ERKKTRClover (Addgene plasmid no. 59150, a gift from M. Covert)[23]. Vectors were packaged using the Lenti-X HTX Packaging System (Clontech) according to the manufacturer's protocols. KP or iKras cells stably expressing ERK-KTR, referred to as KP ERK-KTR or iKras ERK-KTR, respectively, were selected with growth media containing 10 µg ml^{-1} puromycin (Invitrogen) for 7 d and subsequently sorted for cells with high expression of fluorescent proteins via fluorescence activated cell sorting (FACS, MGH Flow Cytometry Core).

BxPC-3 cells transiently expressing *Kras*^{G12D} mutation were generated by transfecting parental BxPC-3 cells with pBabe-Kras^{G12D} plasmid (Addgene plasmid no. 58902, a gift from C. Der) using the Lipofectamine 3000 system (Invitrogen) according to the manufacturer's protocols. As a control, parental BxPC-3 were transfected, again using Lipofectamine 3000, with pBabe-Kras Wt plasmid (Addgene, plasmid no. 75282, a gift from C. Der).

In vitro drug uptake and fluorescent microscopy. To quantify nab-PTX, cross-linked nab-PTX, PLGA-PEG NP or 70 kDa dextran cellular uptake, 7000 MCF10A, H1838, BxPC-3, CT26, Mia, AsPC-1, OVA, LS 180, HT-1080, MDA, A-375, ATC, Raw, BMDM, KP or iKras cells were seeded in each well of a 96-well tissue-culture treated image plates (ibidi). After overnight incubation, cells were treated with 5 µg ml^{-1} fluorescently labelled nab-PTX (nab-PTX-A555 or nab-A555-SiR-taxane; both containing roughly 0.5 µg ml^{-1} PTX), 5 µg ml^{-1} (roughly 0.5 µg ml^{-1} PTX) cross-linked nab-A555-SiR-taxane, 6 µg ml^{-1} PLGA-PEG NP-BODIPY-TMR or 100 µg ml^{-1} fluorescently labelled 70 kDa dextran (70 kDa dextran-A647) for 4 h. The cells were then washed five times with ice-cold PBS and fixed with 4% para-formaldehyde (PFA, EMS) for subsequent fluorescent microscopy imaging or fluorescent detection by plate reader (Tecan). When appropriate, KP or iKras cells were treated with various pharmaceutical inhibitors for 6 h (for EIPA) to 24 h before treatment with fluorescent nab-PTX, cross-linked nab-PTX or 70 kDa dextran. These inhibitors include: 50–100 µM EIPA, 5 µM compound C, 100 nM cobimetinib, 100 nM refametinib, 100 nM MK-8353, 100 nM SCH772984, 1 nM–10 µm trametinab, CFI-40095, AXL1717, VX-745, AZD-7762, JNK-IN-8, ACD-1390, Bindarit, MK-8033, RepSox, 7rh, Y-27632, C021, AS602801, linsitinib and/or A-769662. To assess the effects of glucose deprivation on nab-PTX or cross-linked nab-PTX uptake, iKras cells were washed with PBS and treated with DMEM low glucose medium (containing 1 g l^{-1} D-glucose, Invitrogen) or DMEM high-glucose medium (containing 4.5 g l^{-1} D-glucose, Invitrogen), both supplemented with 10% foetal bovine serum, 100 IU penicillin, 100 µg ml^{-1} streptomycin and 2 µg ml^{-1} doxy, for 24 h before the addition of fluorescently labelled nab-PTX or cross-linked nab-PTX. To evaluate the effects of *Kras* mutation on nab-PTX uptake, iKras cells were washed with PBS and cultured in DMEM/F12 growth media containing no doxy for 48 h or 5 d before fluorescent nab-PTX treatment. In some experiments, KP cells were treated with 10 µg ml^{-1} DQ-Red-BSA or 70 kDa FITC-dextran for 6 h before treatment with fluorescent nab-PTX. In some experiments, to visualize the effects of pharmaceutical inhibition on MAPK pathway activity, KP ERK-KTR or iKras ERK-KTR cells were used. To label endosomes and lysosomes, KP cells were transduced overnight with RAB5A-GFP, RAB7A-GFP or LAMP1-GFP fusion proteins using BacMam 2.0 reagents (Invitrogen) according to the manufacturer's protocols, before drug treatment.

To visualize the nucleus, the fixed samples were counter-stained with 5 µg ml^{-1} 4,6-diamidino-2-phenylindole (DAPI) (Invitrogen). When appropriate, the fixed KP and iKras cells were stained with 1 µg ml^{-1} anti-IGF1 receptor antibody (Clone no. EPR19322, Abcam) followed by appropriate secondary antibody conjugated to A488 (Invitrogen). The fluorescent images of drugs, subcellular compartments, and the ERK-KTR signals inside the cells were captured with a DeltaVision (Applied Precision) modified Olympus BX63 microscope fitted with a Neo sCMOS monochrome camera (Andor).

In vitro drug efficacy study. Here, 3,000 KP or iKras cells were seeded in each well of 96-well plates (Costar). After overnight incubation, cells were treated with various regimens of drugs or dimethylsulfoxide (DMSO) vehicle control. To assess the effects of KRAS mutation on nab-PTX cytotoxicity, iKras cells were cultured without the addition of doxy in the growth media for 24 h, followed by the treatment of various concentrations of nab-PTX for 48 h. For evaluating the effects of trametinab on the efficacy of nab-PTX or sb-PTX, KP or iKras cells were treated with 1–100 nM of trametinab and various concentrations of nab-PTX or sb-PTX together for 48 h (cotreatment). This cotreatment regimen was compared to the Sep-treatment regimen, in which cells were first treated with various concentration of nab-PTX or sb-PTX for 24 h followed by PBS wash-out and further treatment of 1–100 nM trametinab for an additional 24 h. To assess the effects of AXL1717, linsitinib or A-769662 on nab-PTX or sb-PTX cytotoxicity, iKras cells were first pretreated with 1 µM AXL1717, 1 µM linsitinib or 100 nM A-769662 for 24 h, followed by PBS wash-out and further treatment with various concentrations of nab-PTX or sb-PTX for an additional 24 h. This treatment regimen was compared to the regimen in which cells were first treated with nab-PTX or sb-PTX for 24 h, followed by PBS wash-out and further treatment of 1 µM AXL1717, 1 µM Linsitinib or 100 nM A-769662 for an additional 24 h. In some experiments, nab-PTX was added with equal-molar of gemcitabine. Appropriate single-agent (that is, nab-PTX, trametinab or AXL1717 and so on) control experiments using matched dosing timings were performed for all drugs evaluated. For all cytotoxicity experiments, all drugs were washed out 48 h after the initiation of treatment and the cells were cultured for a further 24 h before the assessment of viability using PrestoBlue (Invitrogen) and a plate reader (Tecan) according to the manufacturer's protocol. IC_{50} was determined from the cytotoxicity curve, obtained from non-linear fit of the data using Prism v.7.0 (GraphPad Software). In some in vitro experiments, PTX dissolved in DMSO or Cremophor-EL:ethanol mixture (sb-PTX) was used instead of nab-PTX.

Animal studies and tumour growth evaluation. Unless otherwise noted, experiments were performed using mice that were 6–12 weeks old. To generate KP, iKras or ATC lung tumour models, 2.5×10^5 KP, 1.0×10^5 iKras or 1.0×10^5 ATC cancer cells in 100 µl PBS were injected i.v. via tail-vein catheter into female C57BL/6 mice (for KP and iKras tumour models) or B6129SF1/J mice (for ATC tumour model). The animals were euthanized and lungs harvested for imaging 15 d for iKras lung tumour model, or 30 d for KP and ATC lung tumour models, following tumour inoculation. For s.c. tumour models, 1.0×10^6 KP, iKras or ATC cells in 100 µl PBS were s.c. injected in the flanks of C57BL/6 mice (for KP and iKras tumour models) or B6129SF1/J mice (for ATC tumour model). Imaging or tumour growth evaluation was performed approximately 1–2 weeks postinoculation when the s.c. tumours reached a palpable size (roughly 5 mm in diameter). When indicated, KP cells or ATC cells expressing eGFP or ERK-KTR, or iKras cells expressing H2B-mApple, were used. The mice bearing iKras tumours were fed with water containing 2 g l^{-1} doxy and 20 g l^{-1} sucrose to maintain the expression of *Kras*^{G12D} mutation in the cancer cells. To generate autochthonous KP lung adenocarcinoma, 129KP mice were infected with adenovirus expressing Cre recombinase (AdCre, University of Iowa Viral Vector Core) via intranasal instillation[18]. Lung tumours developed spontaneously and are detectable via magnetic resonance imaging (MRI) 8–12 weeks after viral infection of 129KP mice, at which points these mice were used for imaging experiments. When necessary, all mice were anaesthetized with 2% isoflurane supplied with 2 l min^{-1} O_2 on a heated stage. In all experiments, subjects were monitored daily and any animal reaching humane endpoint, as defined by IACUC, was euthanized. No treatment-related toxicities were observed that triggered >15% loss in body weight or any of the above criteria.

One million iKras cells (for Fig. 4f,g and Supplementary Figs. 12 and 13) or 0.5 million iKras cells (for Fig. 6d–g and Supplementary Figs. 21 and 22) in 100 µl of PBS were implanted s.c. into the flanks of C57BL/6 mice. iKras s.c. tumours were allowed to grow to roughly 50 mm^3 before the initiation of the treatment. Before treatment, the mice were assigned to each cohort to ensure average tumour volume and body weight were matched across all cohorts. When necessary, tumour growth experiments were performed in cohort batches with control group representation in each batch. For trametinib treatment, the mice were given 0.2–0.5 mg kg^{-1} trametinib (Supplementary Tables 1 and 2), dissolved in 1% methylcellulose and 0.2% tween 80, by oral gavage (o.g.) as previously published[54]. For AXL1717 treatment, 15–37.5 mg kg^{-1} AXL1717 (Supplementary Tables 3 and 4), dissolved in 100 µl of mixture of 10% DMSO and 90% olive oil (Sigma), was administered via intraperitoneal (i.p.) injection as described previously[55]. For nab-PTX treatment, 15 mg kg^{-1} nab-PTX in 100 µl of PBS was administered via i.v. injection. For sb-PTX treatment, 15 mg kg^{-1} PTX was dissolved first in a mixture of Cremophor-EL (Sigma) and ethanol (1:1 by volume), and further diluted in 100 µl of PBS for i.v. administration. The tumour-bearing mice received treatments of nab-PTX, sb-PTX, AXL1717, trametinab or appropriate combinations according to various treatment schemes (Supplementary Tables 1–4). Tumour volumes ($V = 0.5 \times \text{width}^2 \times \text{length}$) and mice weight were monitored daily

for up to 2 weeks following the initiation of the treatment using a digital caliper and scale, respectively. Animals were killed when reaching the humane endpoint as defined by IACUC regulations, and the values for tumour volumes at the day of euthanasia were carried over for subsequent days when plotting the tumour growth curves (Fig. 6d and Supplementary Fig. 22a). The tumour growth curves for each group were terminated when half of mice in the group reached humane end-points. Finally, the mice were also monitored for signs of anaphylactic reactions (that is, itching, dyspnoea, paresis, convulsions) on the basis of the clinical score system described previously[56], and no sign was noted. Furthermore, cohorts of immunocompetent C57BL/6 mice were treated with either PBS or nine doses of 15 mg kg^{-1} nab-PTX. Following the treatments, the blood from these mice was collected via terminal cardiac puncture, and incubated undisturbed at 4 °C for 30 min to allow for clotting. The serum was separated from the blood clot by centrifuge at 3,000 r.p.m. for 10 min at 4 °C. Total IgE levels in the mouse serum was then analysed with Mouse IgE ELISA kit (Thermo) according to the manufacturer's protocol. For nab-PTX used in the tumour growth measurement, dosing was calculated on the basis of the amount of PTX payload.

Biodistribution analysis. Here, 15 mg kg^{-1} nab-PTX-A647 (either pharmacy-grade or laboratory-made), 15 mg kg^{-1} Alb-A647, 18 mg kg^{-1} PLGA-PEG NP-BODIPY-TMR or 15 mg kg^{-1} Macrin NP-VT680 in 100 µl of PBS was injected i.v. via tail vein into C57BL/6 mice bearing s.c. KP or iKras tumours, or 129KP mice bearing lung tumours. Then, 24 h postinjection, the animals were euthanized and the tissues were surgically resected, washed in PBS and weighed. The fluorescence intensities of nab-PTX-A647, Alb-A647, PLGA-PEG NP-BODIPY-TMR, Macrin NP-VT680 in the tissue were measured with FRI (A647 λ_{ex} = 650 nm, λ_{em} = 665 nm; VT680: λ_{ex} = 665 nm, λ_{em} = 688 nm; BODIPY-TMR λ_{ex} = 545 nm, λ_{em} = 570 nm) using an OV110 system (Olympus). Average fluorescence intensity for each tissue was determined using Fiji (National Institutes of Health (NIH)), and was background subtracted with auto-fluorescence from corresponding tissue of animals treated with vehicle control (PBS). Percentage of injected dose per gram tissue (% ID per g) was calculated using standards prepared with varying doses of nab-PTX-A647, Macrin NP-VT680 or PLGA-PEG NP-BODIPY-TMR in 1.0% intralipid (McKesson). For nab-PTX-A647, standards were digested in pepsin (pH 4; 37 °C; pepsin:nab, 1:100 by weight) to control for fluorescence dequenching due to cellular catabolism. When appropriate, 100 µg of Rhodamine-labelled Lectin I (Rho-Lectin, Vector Labs) in 100 µl of PBS was injected i.v. via tail vein into the animals 30 min before euthanasia. Rho-Lectin intensity was assessed with fluorescent reflectance imaging (Rho-Lec: λ_{ex} = 550 nm, λ_{em} = 575 nm). In some experiments, the fluorescent intensities of nab-PTX, Alb, PLGA-PEG NP, Macrin NP and Lectin in tumours were assessed with confocal microscopy instead of fluorescent reflectance imaging (next section).

To assess the effects of Kras^{G12D} expression on the biodistribution of nab-PTX-A647 and PLGA-PEG NP-BODIPY-TMR, doxycycline was withdrawn from the feed water of the animals 1 or 4 d before NP injection (2 or 5 d before tissue harvesting). For the assessment of the effects of trametinib, animals were treated with 0.2 mg kg^{-1} trametinib in 1% methylcellulose and 0.2% tween 80 via oral gavage for 4 h, 1 d or 4 d before NP injection (1, 2 or 5 d before tissue harvesting). For assessing the effects of fasting on nab-PTX uptake, animals were fed a water-only diet for 1 d before NP injection. Finally, for the assessment of the effects of AXL1717, animals were treated with 15 mg kg^{-1} AXL1717, dissolved in 100 µl of mixture of 10% DMSO and 90% olive oil, via i.p. injection for 8 h, 1 d or 4 d before NP injection (1, 2 or 5 d before tissue harvesting).

In vivo drug competition experiment. To ascertain whether laboratory-made fluorescent conjugated of nab-PTX (nab-A555-SiR-taxane) and the pharmacy-grade nab-PTX (Abraxane, McKesson) share the same drug target in vivo, a drug competition experiment was performed. Briefly, 1 million KP-GFP cancer cells were implanted s.c. into female C57BL/6 mice. Three weeks following tumour implantation, the mice were administered i.v. with unlabelled pharmacy-grade nab-PTX (3 or 15 mg kg^{-1}) or vehicle control in PBS. Two hours later, laboratory-made fluorescent version of nab-PTX (nab-A555-SiR-taxane) in PBS was injected i.v. Then, 24 h following the fluorescent nab-PTX injection, the mice were perfused with 20 ml of PBS by cardiac puncture and tumours were excised and immediately imaged for SiR-taxane and nab-A555 by confocal microscopy.

Whole-organ optical clearing. Confocal imaging of tumours was performed with optically cleared samples. Here, 30 mg kg^{-1} of nab-A555-SiR-taxane, 15–30 mg kg^{-1} of pharmacy-grade nab-PTX-A647, nab-PTX-A488 or nab-PTX-A555, 18 mg kg^{-1} of BODIPY-TMR labelled PLGA-PEG NP (PLGA-PEG NP-BODIPY-TMR), 10 mg kg^{-1} of Doxil, 41.25 mg kg^{-1} of CDNP-A555, 29 mg kg^{-1} of Lip-DiI or 15 mg kg^{-1} of Alb-A488 in 100 µl PBS was injected into the animal i.v. via tail vein 24 h before euthanasia and tissue extraction. For Cremophor-EL formulation of SiR-taxane (sb-PTX), 30 mg kg^{-1} of SiR-taxane was first dissolved in a mixture of Cremophor-EL (Sigma) and ethanol (1:1 by volume), and further diluted in 100 µl PBS for i.v. administration. When appropriate, 37 mg kg^{-1} Macrin NP-VT680 or 10 mg Fe per kg CLIO-VT680 in 100 µl of PBS was injected to label macrophages 18 h before tissue extraction, while 100 µg Rho-Lec in 100 µl PBS was injected to label blood vessels 1 h before tissue extraction. Mice were then anaesthetized and slowly perfused with 20 ml of PBS followed by 10 ml of 4% PFA via cardiac puncture. Immediately before perfusion, 1 U of Heparin was injected to prevent the coagulation of the blood. Then, s.c. tumours or lungs were excised and further fixed in 4% PFA at 4 °C overnight. The air bubbles in lungs were removed with a brief application of vacuum. For optical clearing, the fixed tissues were placed into a modified CUBIC solution[19] and rocked for 2–3 d at 37 °C. Nuclei were labelled with 5 µg ml^{-1} of DAPI dissolved directly into the CUBIC solution. The tissues were then placed into a microscopy-grade glass chamber filled with fresh CUBIC solution before confocal imaging. No noticeable decreases in fluorescent intensities of all fluorescent moieties, especially SiR-taxane, were observed after the tissue clearing.

Modified CUBIC solution is composed of 27 wt% Urea (Sigma), 27 wt% *N*,*N*,*N*′,*N*′-tetrakis(2-hydroxypropyl)ethylenediamine (quadrol, Sigma), 16 wt% Triton X-100 (Sigma), 30 wt% water and was prepared according to published protocol[19]. Briefly, 125 g of quadrol and 125 g of urea were mixed in 144 g of water. The mixture was stirred at 50 °C until the solid dissolved. The homogenous mixture was then allowed to cool before the addition of 75 g of Triton X-100.

Confocal microscopy. Confocal microscopy was performed with a FluoView FV1000 multi-photon confocal imaging system (Olympus). For confocal microscopy imaging of excised and cleared tissues, an XLFluor ×2 air objective (numerical aperture (NA), 0.14, Olympus) was used for low-magnification imaging, while an XLUMPLFLN ×20 water immersion objective (NA, 1.0, Olympus) was used for high-magnification imaging. Four fluorescent channels were imaged. DAPI, GFP/A488, A555/Rhodamine/BODIPY-TMR, A647/VT680/SiR signals were excited sequentially with 405, 473, 559 and 635-nm diode lasers, respectively, in combination with DM405, 473, 559 and 635-nm dichroic beam splitters. The emitted light was separated with SDM473/560/640-nm beam splitters. DAPI, GFP/A488, A555/Rhodamine/BODIPY-TMR, A647/VT680/SiR signals were detected with BA430-455, BA490-540, BA575-620 and BA655-755-nm emission filters, respectively. Each fluorescence channel was imaged sequentially using distinct excitation and emission filter sets to ensure minimal bleed-through between channels. All lasers, beam splitters and emission filters were purchased from Olympus. Images were collected at 150 or 10 µm intervals in the *z* direction for low or high-magnification imaging, respectively.

Computation of MAPK and AMPK activity scores. To evaluate the relationships between the activities of MAPK or AMPK pathway and nab-PTX uptake, we computed MAPK or AMPK activity output score for cancer-cell lines harbouring different *RAS* and *RAF* mutation states (H1838, BxPC-3, HT-1080, Ls180, MiaPaCa2, AsPC-1, MDA-MB-231 and A-375). Sets of genes whose expressions are controlled by and strongly correlated with MAPK and AMPK activities (MAPK or AMPK signature) were identified from previous studies (Supplementary Table 5)[32,33]. All genes in the MAPK signature are involved in cell proliferation, migration or negative feedback regulation of ERK, while all genes in AMPK signatures are involved in cell metabolism. The mRNA expression level of each of these genes was obtained from publicly available RNA-seq data from Cancer Cell Line Encyclopedia (CCLE)[57]. For each cell line analysed, an average MAPK or AMPK activity score was computed as averaged expression level of all the genes in MAPK or AMPK signature set, respectively. The averaged MAPK or AMPK activity score was plotted against nab-PTX uptake for each cell line for comparison.

Quantification and statistical analysis. *Image analysis.* Imaging data were acquired via Olympus FluoView FV1000 multi-photon confocal microscope or BX63 epifluorescence microscope operating on FV10-SW (Olympus) or MetaMorph software v.7.8.6.0 (Molecular Devices), respectively. We analysed images using Fiji v.2.0.0 (NIH) or MATLAB R2019 (Mathworks). When appropriate, maximum intensity *z* projections of the images were generated. Wide-field images of cleared whole lung or tumour were generated by stitching a 5×5 grid of low-magnification images obtained using a ×2 objective. Automatic thresholding, using the RenyEntropy method, and watershed segmentation were used to generated region of interest to define the boundaries of cancer cells (from GFP signals), macrophages (from CLIO-VT680 or Macrin NP-VT680 signals) or tissues (from DAPI signals). The average fluorescence intensity of drugs (for example, fluorescent nab-PTX) was quantified for each region of interest and either background subtracted (in arbitrary unit, AU) or normalized to background fluorescence intensity (fold increase over background, displayed as normalized intensity, norm. int.). When appropriate, these intensities were further normalized to fluorescent intensities of control groups in each experiment (displayed as fraction control, frac. ctrl.; or fold increase over control, fold inc. over ctrl.). Intensity values in images are directly cross-comparable when corresponding data are displayed on the same graph (for instance, as shown in Figs. 2a or 2g). However not all intensities were normalized to the same base values across different experiments (for example, SiR-taxane in Supplementary Fig. 2a), and cross-comparing absolute intensities is inappropriate in such cases. Similarly, representative fluorescent images that are not in the same figure panel may be displayed with different exposure settings, and cross-comparing between data from different figure panels is inappropriate in such cases. In certain experiments, the uptake of fluorescent nab-PTX is assessed via measuring the

intensity of fluorescently labelled nab vehicle (that is, nab-A555). When possible, the images were randomized before analysis and the investigators were blinded to the identity of the sample from which the images were obtained. In particular, relative cellular uptakes of nab-PTX, PLGA-PEG NP, CDNP, liposome, MNP and Doxil (Fig. 1g) were quantified in this study by measuring the fluorescent intensities of NPs in cancer cells and macrophages in the cleared tissues, according to the following formula:

$$R_{\text{cancer}} = I_{\text{cancer}}/(I_{\text{cancer}} + I_{\text{macrophages}})$$

$$R_{\text{macrophage}} = 1 - R_{\text{cancer}}$$

where I_{cancer} is the fluorescent intensity of NP in cancer cells; $I_{\text{macrophage}}$ is the fluorescent intensity of NP in macrophages; R_{cancer}, relative cellular uptake of cancer cells and $R_{\text{macrophage}}$ is the relative cellular uptake of macrophages.

The relative uptake of ferumoxytol MNP in cancer cells versus macrophages in KP s.c. tumour model, as well as the relative uptake of PLGA-PEG NP in ATC lung tumour model, was derived from data collected in previous studies[58,59].

Statistical analysis. All measurements are taken from biological replicate samples, and results are displayed as mean ± standard error of mean (s.e.m.) unless otherwise noted. All data analyses were performed in Excel 16.45 (Microsoft) or Prism 7.0 (GraphPad Software). A P value of less than 0.05 was deemed statistically significant, while a P value greater than 0.05 was deemed not statistically significant. Statistical tests, including two-tailed Student's t-test, one-way analysis of variance (ANOVA) test with Tukey, Dunnett or Holm-Sidak post test for multiple comparison, Spearman correlation test, Pearson correlation test (to obtain Pearson's R value and two-tailed t-test value) and Wilcoxon log-rank test were performed with Prism v.7.0. The results and the details of the statistical analysis can be found in figure legends. ANOVA tests carried out in this study were followed by post test for multiple comparison, and adjusted P values for multiple comparison were reported for each ANOVA test. Measurements were taken from distinct samples (that is, cells, mice and organs). All data meet the assumptions and criteria for the statistical tests carried out. Furthermore, D'Agostino-Pearson omnibus normality test and F-test were performed using Prism 7.0 when appropriate to ensure data meet the normality and equal variance criteria. Samples were assigned randomly to each experimental group. For each experimental group, three or more independent biological replicates ($n \geq 3$ independent experiments) were performed, and no sample was excluded for analysis. Statistical tests were performed with averaged values calculated from biologically independent samples and experiments (that is, cell cultures, animals). Sample sizes were based on previous studies performed in our laboratory on these and similar experimental models, and chosen to meet the current standard for in vivo and in vitro experiments[48,60]. When possible, the investigators were blinded to the identities of the samples' treatment groups during data analysis.

Materials availability. Further information and requests for resources and reagents should be directed to and will be fulfilled by the lead contact, M.A.M. This study did not generate new unique reagents.

Reporting Summary. Further information on research design is available in the Nature Research Reporting Summary linked to this article.

Data availability

All data are available from corresponding authors upon request. RNA-seq data used to calculate the MAPK/AMPK activity score for each cell line were obtained from the Cancer Cell Line Encyclopedia (https://portals.broadinstitute.org/ccle).

Code availability

This study did not generate new custom code or mathematical algorithms.

References

39. Ying, H. et al. Oncogenic Kras maintains pancreatic tumors through regulation of anabolic glucose metabolism. *Cell* **149**, 656–670 (2012).
40. Dinulescu, D. M. et al. Role of K-ras and Pten in the development of mouse models of endometriosis and endometrioid ovarian cancer. *Nat. Med.* **11**, 63–70 (2005).
41. McAuliffe, S. M. et al. Targeting Notch, a key pathway for ovarian cancer stem cells, sensitizes tumors to platinum therapy. *Proc. Natl Acad. Sci. USA* **109**, E2939–E2948 (2012).
42. McFadden, D. G. et al. p53 constrains progression to anaplastic thyroid carcinoma in a Braf-mutant mouse model of papillary thyroid cancer. *Proc. Natl Acad. Sci. USA* **111**, E1600–E1609 (2014).
43. Vanden Borre, P. et al. Combined BRAF(V600E)- and SRC-inhibition induces apoptosis, evokes an immune response and reduces tumor growth in an immunocompetent orthotopic mouse model of anaplastic thyroid cancer. *Oncotarget* **5**, 3996–4010 (2014).
44. Rodell, C. B. et al. TLR7/8-agonist-loaded nanoparticles promote the polarization of tumour-associated macrophages to enhance cancer immunotherapy. *Nat. Biomed. Eng.* **2**, 578–588 (2018).
45. Vanden Borre, P. et al. The next generation of orthotopic thyroid cancer models: immunocompetent orthotopic mouse models of BRAF V600E-positive papillary and anaplastic thyroid carcinoma. *Thyroid* **24**, 705–714 (2014).
46. Girnita, A. et al. Cyclolignans as inhibitors of the insulin-like growth factor-1 receptor and malignant cell growth. *Cancer Res.* **64**, 236–242 (2004).
47. Mulvihill, M. J. et al. Discovery of OSI-906: a selective and orally efficacious dual inhibitor of the IGF-1 receptor and insulin receptor. *Future Med. Chem.* **1**, 1153–1171 (2009).
48. Miller, M. A. et al. Tumour-associated macrophages act as a slow-release reservoir of nano-therapeutic Pt(IV) pro-drug. *Nat. Commun.* **6**, 8692 (2015).
49. Pineda, J. J. et al. Site occupancy calibration of taxane pharmacology in live cells and tissues. *Proc. Natl Acad. Sci. USA* **115**, E11406–E11414 (2018).
50. Devaraj, N. K., Keliher, E. J., Thurber, G. M., Nahrendorf, M. & Weissleder, R. 18F labeled nanoparticles for in vivo PET-CT imaging. *Bioconjug Chem.* **20**, 397–401 (2009).
51. Josephson, L., Tung, C. H., Moore, A. & Weissleder, R. High-efficiency intracellular magnetic labeling with novel superparamagnetic-Tat peptide conjugates. *Bioconjug Chem.* **10**, 186–191 (1999).
52. Langer, K. et al. Optimization of the preparation process for human serum albumin (HSA) nanoparticles. *Int. J. Pharm.* **257**, 169–180 (2003).
53. Langer, K. et al. Human serum albumin (HSA) nanoparticles: reproducibility of preparation process and kinetics of enzymatic degradation. *Int. J. Pharm.* **347**, 109–117 (2008).
54. Tsubaki, M. et al. Trametinib suppresses chemotherapy-induced cold and mechanical allodynia via inhibition of extracellular-regulated protein kinase 1/2 activation. *Am. J. Cancer Res.* **8**, 1239–1248 (2018).
55. Menu, E. et al. Inhibiting the IGF-1 receptor tyrosine kinase with the cyclolignan PPP: an in vitro and in vivo study in the 5T33MM mouse model. *Blood* **107**, 655–660 (2006).
56. Xu, W., Tamura, T. & Takatsu, K. CpG ODN mediated prevention from ovalbumin-induced anaphylaxis in mouse through B cell pathway. *Int. Immunopharmacol.* **8**, 351–361 (2008).
57. Barretina, J. et al. The Cancer Cell Line Encyclopedia enables predictive modelling of anticancer drug sensitivity. *Nature* **483**, 603–607 (2012).
58. Ng, T. S. C. et al. Detecting immune response to therapies targeting PDL1 and BRAF using ferumoxytol MRI and Macrin in anaplastic thyroid cancer. *Radiology* **298**, 123–132 (2020).
59. Miller, M. A. et al. Predicting therapeutic nanomedicine efficacy using a companion magnetic resonance imaging nanoparticle. *Sci. Transl. Med.* **7**, 314ra183 (2015).
60. Miller, M. A. et al. Radiation therapy primes tumors for nanotherapeutic delivery via macrophage-mediated vascular bursts. *Sci. Transl. Med.* **9**, eaal0225 (2017).

Acknowledgements

We acknowledge S. Schmidt and G. Wojtkiewicz for assistance with imaging and biodistribution through the MGH-CSB MIP program. Part of this work was supported by NIH/NCI grant nos. R00CA207744 (M.A.M), DP2CA259675 (M.A.M), U01CA206997 (R.W.), R01HL131495 (R.W.), R01CA206890 (R.W.), T32CA079443 (R.L.), R01GM069668 (D.A.L.), R01CA96504 (D.A.L.), U54CA112967 (D.A.L.), U54CA217377 (D.A.L.), the NSF Graduate Research Fellowship Program (S.J.W.), the American Cancer Society-Ellison Foundation Postdoctoral Fellowship PF-20-106-01-LIB (R.L.), MGH FMD Fellowship (R.L.) and an American Thyroid Association/Thyroid Cancer Survivors' Association Research Grant (T.S.C.N.).

Author contributions

R.L., R.W. and M.A.M. developed the concept. R.L., T.S.C.N., S.J.W., C.B.R., H.M., N.B., R.W. and M.A.M designed the experiments. R.L., T.S.C.N., S.J.W, M.P., C.B.R, H.M., R.H.K. and M.A.G. performed the experiments. R.L., R.W. and M.A.M. wrote the paper. R.L., T.S.C.N., S.J.W., M.P., C.B.R., H.M., R.H.K., M.A.G., D.A.L., S.P., D.M.D., N.B., R.W. and M.A.M. analysed the results and edited the paper.

Competing interests

R.W. is a cofounder of T2Biosystems and Lumicell, serves as a scientific adviser for ModeRNA Therapeutics, Tarveda Therapeutics and Alivio Therapeutics. None of these activities are related to the paper. The other authors declare that they have no competing interests.

Additional information

Supplementary information The online version contains supplementary material available at https://doi.org/10.1038/s41565-021-00897-1.

Correspondence and requests for materials should be addressed to R.W. or M.A.M.

Peer review information *Nature Nanotechnology* thanks Twan Lammers and the other, anonymous, reviewer(s) for their contribution to the peer review of this work.

Reprints and permissions information is available at www.nature.com/reprints.

nature research

Corresponding author(s): Miles A. Miller and Ralph Weissleder

Last updated by author(s): Feb 18, 2021

Reporting Summary

Nature Research wishes to improve the reproducibility of the work that we publish. This form provides structure for consistency and transparency in reporting. For further information on Nature Research policies, see our Editorial Policies and the Editorial Policy Checklist.

Statistics

For all statistical analyses, confirm that the following items are present in the figure legend, table legend, main text, or Methods section.

n/a	Confirmed	
☐	☒	The exact sample size (*n*) for each experimental group/condition, given as a discrete number and unit of measurement
☐	☒	A statement on whether measurements were taken from distinct samples or whether the same sample was measured repeatedly
☐	☒	The statistical test(s) used AND whether they are one- or two-sided *Only common tests should be described solely by name; describe more complex techniques in the Methods section.*
☐	☒	A description of all covariates tested
☐	☒	A description of any assumptions or corrections, such as tests of normality and adjustment for multiple comparisons
☐	☒	A full description of the statistical parameters including central tendency (e.g. means) or other basic estimates (e.g. regression coefficient) AND variation (e.g. standard deviation) or associated estimates of uncertainty (e.g. confidence intervals)
☐	☒	For null hypothesis testing, the test statistic (e.g. *F*, *t*, *r*) with confidence intervals, effect sizes, degrees of freedom and *P* value noted *Give P values as exact values whenever suitable.*
☒	☐	For Bayesian analysis, information on the choice of priors and Markov chain Monte Carlo settings
☒	☐	For hierarchical and complex designs, identification of the appropriate level for tests and full reporting of outcomes
☐	☒	Estimates of effect sizes (e.g. Cohen's *d*, Pearson's *r*), indicating how they were calculated

Our web collection on statistics for biologists contains articles on many of the points above.

Software and code

Policy information about availability of computer code

Data collection	Imaging data were acquired via Olympus FluoView FV1000 multi-photon confocal microscope or BX63 epifluorescence microscope operating on FV10-SW (Olympus) or MetaMorph softwares 7.8.6.0 (Molecular Devices), respectively.
Data analysis	Image analysis was performed with Fiji 2.0.0 (NIH) or Matlab R2019 (Mathworks). All data analyses were performed in Excel 16.45 (Microsoft) or Prism 7.0 (GraphPad Software). All statistical tests were performed with Prism 7.0.

For manuscripts utilizing custom algorithms or software that are central to the research but not yet described in published literature, software must be made available to editors and reviewers. We strongly encourage code deposition in a community repository (e.g. GitHub). See the Nature Research guidelines for submitting code & software for further information.

Data

Policy information about availability of data

All manuscripts must include a data availability statement. This statement should provide the following information, where applicable:

- Accession codes, unique identifiers, or web links for publicly available datasets
- A list of figures that have associated raw data
- A description of any restrictions on data availability

All data are available from corresponding authors upon request. RNA seq data used to calculate MAPK/AMPK activity score for each cell line were obtained from Cancer Cell Line Encyclopedia (https://portals.broadinstitute.org/ccle).

Field-specific reporting

Please select the one below that is the best fit for your research. If you are not sure, read the appropriate sections before making your selection.

☒ Life sciences ☐ Behavioural & social sciences ☐ Ecological, evolutionary & environmental sciences

For a reference copy of the document with all sections, see nature.com/documents/nr-reporting-summary-flat.pdf

Life sciences study design

All studies must disclose on these points even when the disclosure is negative.

Sample size	Sample sizes were based on previous studies performed in our laboratory on these and similar experimental models, and chosen to meet the current standards for in vivo and in vitro experiments. Previous studies: Miller, M. A. et al. Tumour-associated macrophages act as a slow-release reservoir of nano-therapeutic Pt(IV) pro-drug. Nat Commun 6, 8692 (2015). Miller, M. A. et al. Radiation therapy primes tumors for nanotherapeutic delivery via macrophage-mediated vascular bursts. Sci Transl Med 9, (2017). Rodell, C. B. et al. TLR7/8-agonist-loaded nanoparticles promote the polarization of tumour-associated macrophages to enhance cancer immunotherapy. Nat Biomed Eng 2, 578-588 (2018).
Data exclusions	No sample or data was excluded for analysis
Replication	For all our analyses, we performed experiments across at least 3 biological replicates, all of which were included in our analyses. All attempts at replication were successful.
Randomization	For all in vitro experiments, samples were assigned randomly to each experimental group. For all in vivo experiments, animals (litter-mate) were randomly assigned to each experimental group prior to treatment.
Blinding	When possible, investigators were blinded to the identities of the samples' treatment group during data analysis.

Reporting for specific materials, systems and methods

We require information from authors about some types of materials, experimental systems and methods used in many studies. Here, indicate whether each material, system or method listed is relevant to your study. If you are not sure if a list item applies to your research, read the appropriate section before selecting a response.

Materials & experimental systems

n/a	Involved in the study
☐	☒ Antibodies
☐	☒ Eukaryotic cell lines
☒	☐ Palaeontology and archaeology
☐	☒ Animals and other organisms
☒	☐ Human research participants
☒	☐ Clinical data
☒	☐ Dual use research of concern

Methods

n/a	Involved in the study
☒	☐ ChIP-seq
☒	☐ Flow cytometry
☒	☐ MRI-based neuroimaging

Antibodies

Antibodies used	Rabbit anti-IGF1R primary antibody (Abcam, ab182408, clone#EPR19322); Goat Anti-Rabbit IgG H&L secondary antibody, Alexa Fluor 488 (Invitrogen, A-11034, polyclonal)
Validation	Rabbit anti-IGF1R primary antibody (Abcam ab182408) was validated for immunofluorescent staining by the manufacturer. The product is also knockout validated by manufacturer (https://www.abcam.com/igf1-receptor-antibody-epr19322-ab182408.html).

Eukaryotic cell lines

Policy information about cell lines

Cell line source(s)	NCI-H1838, BxPC-3, CT26, AsPC-1, MiaPaCa-2, LS180, HT-1080, Raw264.7, MDA-MB-231, A-375, and MCF10A were all

Cell line source(s)	obtained from ATCC. KP1.9 mouse lung cancer cells were obtained from Dr. Annette Zippelius (University Hospital Basel). AC37 iKras mouse pancreatic cancer cells were obtained from Dr. Nabeel Bardeesy (MGH). 4306 OVA mouse ovarian cancer cells were obtained from Dr. Daniela Dinulescu (Havard Medical School). 3743 ATC mouse thyroid cancer cells were obtained from Dr. Sareh Parangi (MGH). Bone marrow-derived macrophages were isolated from the femurs of 10 wks old C57BL/6 mice (Jackson Laboratory).
Authentication	Cell lines were not further authenticated after their receipt from ATCC or the source.
Mycoplasma contamination	All cells were tested for mycoplasma contamination using PlasmoTest Mycoplasma Detection Kit (InvivoGen) according to manufacturer's protocols. Negative test results were obtained for all cell lines used.
Commonly misidentified lines (See ICLAC register)	None

Animals and other organisms

Policy information about studies involving animals; ARRIVE guidelines recommended for reporting animal research

Laboratory animals	Experiments were performed using female mice that were 6-12 weeks old. 129S1 mice harboring Cre-activated conditional KrasLSL-G12D/+Trp53flox/flox (129KP mice, a generous gift from Dr. Mikael J. Pittet, MGH) were used as an autochthonous mouse model of non-small cell lung cancer. C57BL/6J (JAX), B6129SF1/J (JAX), and 129KP mice were fed with autoclaved food and water and maintained in ventilated cages in a light-dark cycle, temperature (18-23 °C), and humidity (40-60%) controlled pathogen-free vivarium at MGH.
Wild animals	This study did not involve wild animals.
Field-collected samples	This study did not involve samples collected from the field.
Ethics oversight	Animal research was performed in compliance with guidelines from the Institutional Animal Care and Use Committee (IACUC) at Massachusetts General Hospital (MGH).

Note that full information on the approval of the study protocol must also be provided in the manuscript.